

HREM Study of Compounds in the Bi-Rich Part of the Ba–Bi–O System

V. I. Nikolaichik,* S. Amelinckx,‡ L. A. Klinkova,† N. V. Barkovskii,† O. I. Lebedev,‡,1 and G. Van Tendeloo‡

**Institute of Microelectronics Technology and High Purity Materials, Russian Academy of Sciences, Chernogolovka, Moscow District 142432, Russia;* †*Institute of Solid State Physics, Russian Academy of Sciences, Chernogolovka, Moscow District 142432, Russia;* and ‡*EMAT, University of Antwerp (RUCA), Groenenborgerlaan 171, B-2020 Antwerpen, Belgium*

Received May 16, 2001; in revised form August 8, 2001; accepted August 16, 2001; published online November 27, 2001

A series of perovskite-like compounds with general composition $Ba_nBi_{n+m}O_y$ (m, n —integer) has been studied by means of electron diffraction and high-resolution electron microscopy. For a number of simple, discrete values of the cation composition ratio Ba:Bi the structures were found to be Ruddlesden–Popper-like derivatives of the perovskite structures of $BaBiO_3$, with composition-dependent long periods. For more complicated values of the cation composition ratio the perovskite blocks are further fragmented by planar interfaces into a two-dimensional periodic island structure. This fragmentation gives rise to complicated local structures formed by a mosaic of square or (and) rectangular islands, which often produce incommensurate diffraction patterns. Such diffraction patterns are interpreted in the framework of the “fractional shift” method for interface modulated structure. Structure models and compositions can be made compatible by assuming that substitution of barium ions by bismuth ions must take place, predominantly along the island boundaries. © 2002 Elsevier Science

1. INTRODUCTION

The phase relations in the Ba–Bi–O system attract special attention since this system could be considered as the parent system for such superconductors as $Ba_{1-x}K_xBiO_3$ (1) or $BaBi_{1-x}Pb_xO_3$ (2). The structure of the $BaBiO_3$ compound is closely related to the perovskite structure, but the ordering of Bi^{3+} and Bi^{5+} cations and the cooperative tilting of BiO_6 octahedra result in a monoclinic superstructure (3). The appearance of superconductivity is caused by a cation replacement either in the *A* sublattice or in the *B* positions, resulting in the suppression of the charge ordering at the *B* positions and in the formation of an isotropic cubic structure for $Ba_{1-x}K_xBiO_3$ ($0.37 < x < 0.5$) (4) or of a tetragonal perovskite $BaBi_{0.25}Pb_{0.75}O_3$ (5). The cation

stoichiometry determines the structure and also the transport properties of the compounds in these systems. For all these reasons an investigation of the structural changes in compounds of the Ba–Bi–O system caused by a variation of the cation composition could be a subject of interest.

Investigations of the barium-rich region of the Ba–Bi–O system have shown that the formation of the solid solution $Ba_{1+x}Bi_{1-x}O_3$ ($0 \leq x \leq 0.33$) is associated with the replacement of Bi cations by Ba ones in octahedrally coordinated *B* sites. An increasing concentration of Ba in the *B* sublattice results in a symmetry increase from monoclinic (for $BaBiO_3$) to rhombohedral (for $x = 0.14$) and finally to cubic (for $x = 0.2–0.33$) (6–8). Studies of phase relations in this region have revealed a number of oxides with perovskite-related ordered structures (9, 10).

The formation of a series of $Ba_nBi_{n+m}O_y$ perovskite-related compounds was also reported for the Bi-rich region of the system (10, 11). However, structure information is only available for the $BaBi_3O_{5.5}$ compound (12–14). According to the structure models proposed on the basis of these data, an excess of Bi in comparison with the ideal perovskite composition results in the appearance of rocksalt-type $Bi_2O_{2-\delta}$ blocks followed by the formation of a body-centered unit cell. It is reasonable to suppose that the formation of an intergrowth structure with alternating perovskite blocks and Bi-enriched rocksalt-type layers is a general way to accommodate the Bi excess on going through the row of $Ba_nBi_{n+m}O_y$ compounds.

The aim of this work is to perform a structure study of the compounds with different Ba:Bi ratios and to reveal the common structure trends allowing these compounds to vary the cation composition and the oxygen content.

2. EXPERIMENTAL

The investigated samples were prepared by applying two different techniques: the ceramic method and crystallization

¹To whom correspondence should be addressed.

from the melt, using BaO₂ (99.5%) or Ba(NO₃)₂ (99.5%) and Bi₂O₃ (99.5%) as initial reagents. Stoichiometric amounts of Ba(NO₃)₂ and Bi₂O₃ with cation ratios Ba:Bi = 2:3, 3:5, 1:2, and 4:11 were intimately mixed, pelletized, and heated in argon (residual content of CO₂ and H₂O less than 10⁻⁴ vol.%) at 600 and 700°C for 24 h, both with intermediate regrinding. After final annealing at 880°C (the 2:3 and 3:5 samples), at 780°C (the 1:2 sample), and at 750°C (the 4:11 sample), they were quenched in an Ar atmosphere.

The Ba:Bi = 1:3 samples were of two types. They were prepared by heating a stoichiometric mixture of BaO₂ and Bi₂O₃ in air at 700°C for 24 h followed by liquid nitrogen quenching (the first type) or in argon at 630°C for 24 h followed by quenching in an Ar atmosphere (the second type).

The sample of the composition Ba:Bi = 4:5 was prepared from the stoichiometric mixture of BaO₂ and Bi₂O₃ by the following procedure: annealing at 800°C in air for 18 h, melting at 1000°C, cooling down to 960°C at a rate of 2°C/h, keeping at this temperature for 1 h, and quenching into liquid nitrogen.

The synthesized samples were investigated by X-ray powder diffraction using a Siemens D-500 diffractometer (CuK α_1 radiation). X-ray diffraction patterns make it possible to index only the reflections belonging to the perovskite sublattice, the corresponding cell parameters are given in Table 1. Several weak peaks were also observed in the low-angle region of the X-ray patterns of all the samples; an interpretation of them as supercell reflections proved ambiguous. We will see that the perovskite blocks are fragmented in a superstructure consisting of islands; they may be responsible for these weak reflections. The 4:5 sample was found to be orthorhombic. The increase of Bi content

results in increasing symmetry to tetragonal (samples 2:3, 3:5, 1:2, and 4:11) and then to cubic (1:3 sample) and is accompanied by a decrease of cell volume, in accordance with the ionic radii of Ba²⁺ ($r = 1.42 \text{ \AA}$) and Bi³⁺ ($r = 1.11 \text{ \AA}$).

Iodometric titration (oxidation of Mn²⁺ and I⁻ ions in an acid medium) was used to determine the content of Bi⁵⁺ ions in the 2:3 and 1:2 samples. According to the chemical analysis an average oxidation state of bismuth $V_{\text{Bi}} = + 3.01 - 3.02$ was found.

Samples for transmission electron microscopy experiments were obtained by grinding the crystals in an agate mortar. The powder was suspended in methanol and spread over thin holey carbon films. We used a JEM-2000FX microscope for electron diffraction (ED) and EDX analysis. Sets of X-ray spectra were collected from 30–50 particles exhibiting the same diffraction pattern; the Ba:Bi ratios for the investigated samples given in Table 1 were obtained by averaging over the set. No contamination by Al was found for any of the studied phases. High-resolution electron microscopy (HREM) was performed using a JEOL 4000EX microscope. The image simulations were obtained using the MacTempas software.

3. STRUCTURAL CONSIDERATIONS

3.1. Perovskite-Like Structures

The perovskite structure is one of the most widespread structure types for crystals with compositions ABX_3 where A and B are cations and X are anions. Especially many oxides ($X = \text{O}$) are representatives of this structure type. The A ions together with the oxygen ions form an ordered close-packed arrangement (which may be either cubic or hexagonal) in which the B ions occupy interstices of the corner-sharing “all-oxygen” octahedra. The ideal perovskite structure is represented in Fig. 1a In what follows we will make extensive use of the projected representations of Figs. 1a and 1b.

When viewed along a cube direction the different heavy ions occur in separate columns, which is a favorable feature for HREM imaging (Figs. 1a, 1b). In particular the columns containing A and B cations can, under adequate conditions, be imaged as dots of a different brightness.

Lamellae of perovskite, limited by cube planes, occur in a number of so-called mixed layer compounds, in which the perovskite multilayer lamellae alternate with thin layers of a different type. For instance in the Aurivillius phases perovskite blocks are intergrown with Bi₂O₂ layers of the BiOF type (15). Mixed layer compounds with defective fluorite-type intermediate layers are also known.

We shall see that the compounds studied in this paper are best described as analogues of the Ruddlesden–Popper structure type (16). In these compounds the perovskite blocks alternate with NaCl-type BiO layers. The presence of

TABLE 1
Cell Parameters of the Phases with Different Ba:Bi ratios

Starting Ba:Bi ratio	Cell parameters, \AA	c/a ratio	Cell volume, \AA^3
4:5 (0.80)	$a = 4.381(1)$ $b = 4.355(1)$ $c = 4.505(1)$	—	85.95
2:3 (0.67)	$a = 4.3759(2)$ $c = 4.4834(3)$	1.0246	85.85
3:5 (0.60)	$a = 4.3663(7)$ $c = 4.496(1)$	1.0321	85.71
1:2 (0.50)	$a = 4.3544(3)$ $c = 4.4941(5)$	1.0322	85.21
4:11 (0.36)	$a = 4.3926(3)$ $c = 4.3735(4)$	0.9957	84.39
1:3 (0.33)	$a = 4.3718(3)$	—	83.55

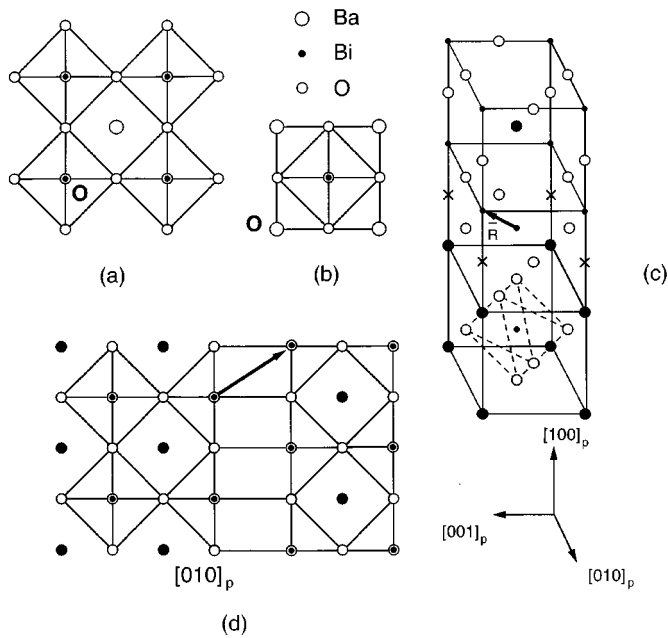


FIG. 1. Schematic representation of the perovskite structure: (a) $[010]_p$ view, the origin \mathbf{O} of the unit cell is in a bismuth position; (b) $[010]_p$ view, the origin \mathbf{O} of the unit cell is in a barium position; (c) spatial view of interface between two different representations; (d) planar interface with displacement vector $\frac{1}{2} [111]_p$ as projected along $[010]_p$.

the NaCl-type layers causes an offset over $\frac{1}{2} [111]$ of successive perovskite blocks (Figs. 2 and 3)

These structures can be considered as periodically faulted perovskite structures; the fault vector being $\frac{1}{2} [111]_p$, and the fault plane being $\{100\}$. Such a fault is represented in space in Fig. 1c in which the crosses represent oxygen positions that can be either occupied or vacant, depending on the oxygen content. The presence of faults of a similar type was assumed in order to explain the occurrence of a body-centered lattice in diffraction patterns of the compound (13). A fault with the same displacement vector $\frac{1}{2} [111]_p$ on a $(100)_p$ -type plane is presented as viewed along $[010]_p$ in Fig. 1d. This is the type of fault on (001) planes suggested by the HREM images to occur periodically in the long-period layered structures (Fig. 3).

3.2. The Fractional Shift Method

The combined observations of HREM images and of diffraction patterns to be discussed below will show that the superstructures result from modulation by periodic planar interfaces of a basic perovskite structure. For a detailed interpretation of the geometry of the diffraction patterns we will make use of the diffraction theory of interface modulated structures (17), which can be summarized by the following expression for the positions of satellite sequences

produced by a one-dimensional interface-modulated structure

$$\mathbf{H} = \mathbf{h} + [m + (\mathbf{h} \cdot \mathbf{R})] \mathbf{q}, \quad [1]$$

with $\mathbf{q} = \mathbf{e}_n/d$. \mathbf{H} is the diffraction vector of the observed superstructure spot (i.e., of a satellite due to the modulated structure); \mathbf{h} is the position of the diffraction spot of the basic structure (i.e., in our case the perovskite structure) with which the satellite is associated; m is the order of the satellite and it is in general a small integer since the intensity of the satellite spots decreases rapidly with increasing order, i.e., with increasing separation from the basic spot; \mathbf{R} is the displacement vector of the interfaces that cause the modulation; it is assumed to be the same for all interfaces in a parallel set. \mathbf{R} is not a lattice vector and $\mathbf{h} \cdot \mathbf{R}$ is thus a fraction and hence causes a “fractional shift” of the satel-

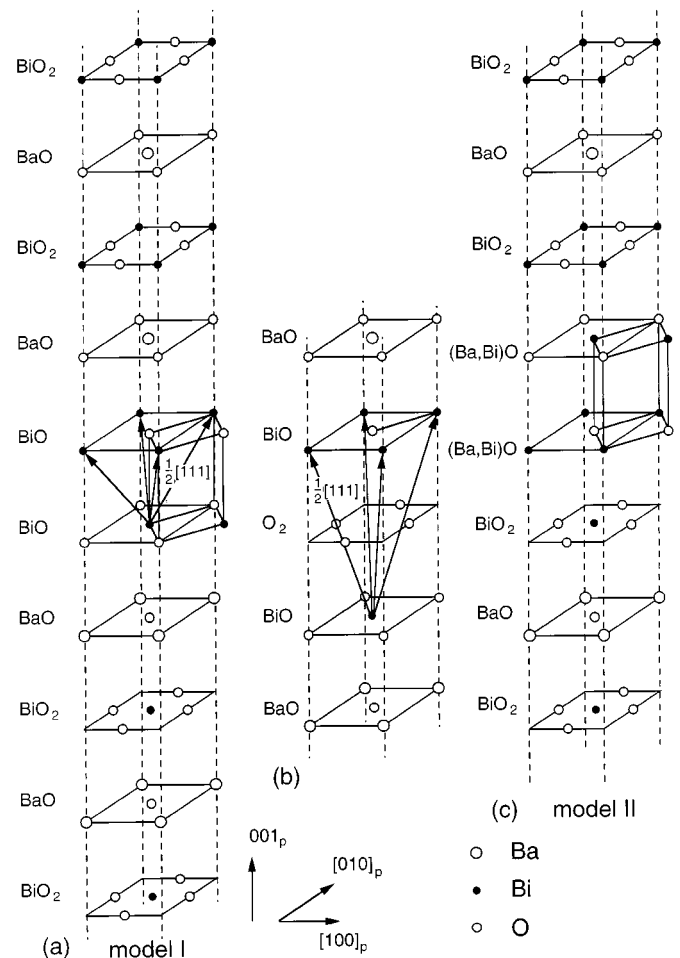


FIG. 2. Expanded view of the assumed layer stacking along $[001]$ in the layered perovskites. In particular the geometry of the planar interface with a displacement vector $\frac{1}{2} [111]$ is shown to follow from the presence of a bilayer BiO in the NaCl configuration in (a) and (c) and possibly of a defective CaF_2 configuration in (b).

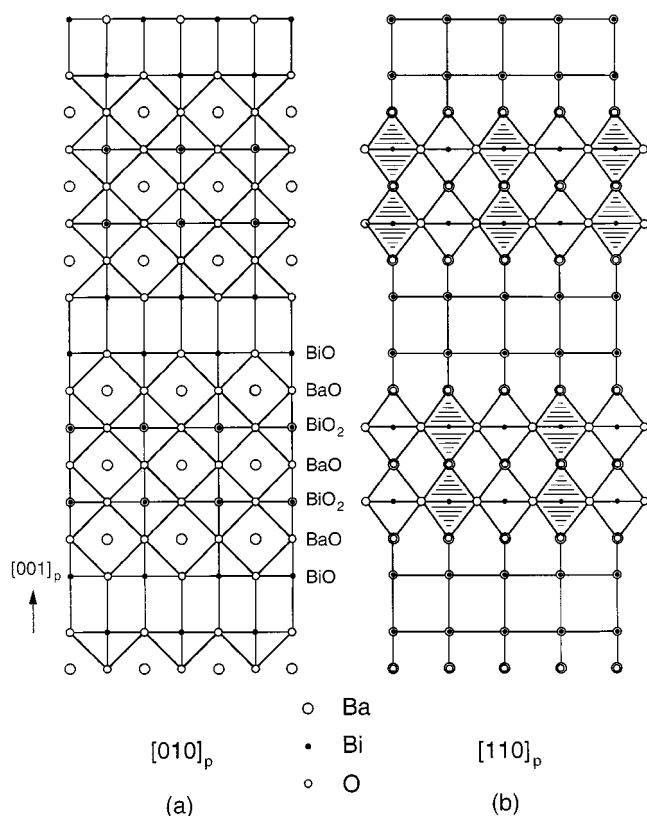


FIG. 3. Structure model of the 7-layered compound with ideal composition $\text{Ba}_3\text{Bi}_4\text{O}_y$. Successive perovskite blocks are related by a displacement $\frac{1}{2} [111]_p$, caused by the presence of NaCl-like bilayers of BiO: (a) $[010]_p$ view; (b) $[110]_p$ view. This model can be compared with the high-resolution image of Fig. 10b.

lite arrays. \mathbf{q} is the modulation vector, which is oriented along the unit normal \mathbf{e}_n on the interfaces and has a length $1/d$, where d is the spacing of the planar interfaces. The relation [1] does not depend on the chosen reference frame, but implies that \mathbf{R} and \mathbf{h} are described with respect to the corresponding direct and reciprocal lattices respectively.

According to the kinematical diffraction theory (18) the intensity distribution along the linear arrays of satellites is described by the slit function $\sin x/x$ with $x = \pi u d$, centered on the basic spot \mathbf{h} ; u measures the distance from the basic spot to the satellite. The intensities thus decrease rapidly with increasing order of the satellites.

It should be noted that the basic spot with diffraction vector \mathbf{h} need not be present and is in fact often absent, but its position can be located since it is a vector of the reciprocal lattice of the basic structure. In a number of cases the interface spacing d is not constant but is in fact a regular mixture of two or more different spacings. In that case the spacing d is meant to be the average $\langle d \rangle$. The planar interfaces need not be strictly confined to simple lattice planes of the basic structure, but systematic sidewise “ledging” may occur. In this case the unit vector \mathbf{e}_n is meant to be

oriented along the normal to the “average” direction of the interface. These complications lead to “incommensurate” diffraction patterns exhibiting either “spacing anomalies” or (and) “orientation anomalies.”

The theory can be extended to include two-dimensional grids of two intersecting sets of parallel interfaces with average spacings d_1 and d_2 . For each set one can define a modulation vector $\mathbf{q}_1 = \mathbf{e}_1/d_1$ and $\mathbf{q}_2 = \mathbf{e}_2/d_2$ and corresponding displacement vectors \mathbf{R}_1 and \mathbf{R}_2 . The fractional shifts caused by the two sets of interfaces now must be superposed since they are independent. The satellite positions \mathbf{H} now form a two-dimensional array arranged around a basic spot \mathbf{h} ; the vectors \mathbf{H} are given by the expression

$$\mathbf{H} = \mathbf{h} + [m_1 + (\mathbf{h} \cdot \mathbf{R}_1)] \mathbf{q}_1 + [m_2 + (\mathbf{h} \cdot \mathbf{R}_2)] \mathbf{q}_2; \quad [2]$$

i.e., the fractional shifts along the two different directions are added as vectors. Each satellite of the planar array is characterized by two integers or “orders,” m_1 and m_2 .

Further generalization to three-dimensionally modulated structures is obvious. It should be noted that in such a case the theory is also applicable in projection. If the considered projection axis is parallel to the direction of the intersection lines of the two sets of interfaces the geometry of the section of reciprocal space along the considered zone is adequately described by the relation [2] where now \mathbf{R}_1 and \mathbf{R}_2 are the projected displacement vectors along the considered zone.

The relations [1] and [2] can clearly be applied to put restrictions on possible displacement vectors since the experimentally observed fractional shifts determine in fact the projections of \mathbf{R} onto \mathbf{h} . However the fractional shifts are only known modulus an integer. This is often sufficient since \mathbf{R} is only determined modulus a lattice vector of the basic structure. Moreover \mathbf{R} is usually restricted to vectors connecting site positions of the basic structure. HREM images are of considerable help in suggesting plausible displacement vectors. Application to the system under discussion is described in Section 5.1.

4. OBSERVATIONS

4.1. Electron Diffraction Patterns

4.1.1. Introductory remarks. As yet the materials have mainly been characterized by powder X-ray diffraction, which unfortunately only allows limited identification of the various local superstructures, since they only differ by subtle details as will be revealed by the single-crystal electron diffraction studies to be discussed here. Limitations of the latter technique stem from the fact that it is often impossible to obtain mutually perpendicular sections of the same reciprocal space, due to the limited tilt range of the microscope specimen holder. Moreover the crystals exhibit a preferential cleavage along the layer plane, so that mostly

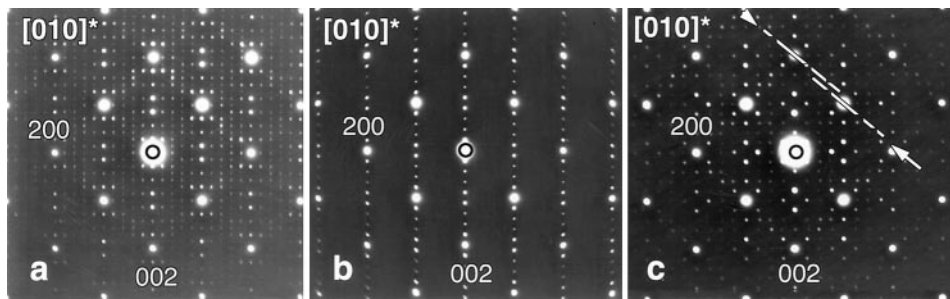


FIG. 4. (a) Electron diffraction pattern of the 7-layered structure along the $[010]$ zone. Spots due to ordering within (001) layers are also present: (b) Electron diffraction pattern of the 9 layer structure along the $[010]$ zone. (c) $[010]$ diffraction patterns of island fragmented 5-layered incommensurate superstructure.

transverse sections are obtained rather than axial sections. As a result it has not always been possible to ascertain that two different patterns refer to the same reciprocal lattice since often the two patterns originate from different grains albeit of the same batch or at least of batches with the same cation ratio Ba:Bi and the same thermal treatment.

Fortunately certain features of the axial sections of a number of specimens also reveal the superperiods in the transverse sections, thus allowing us to conclude whether a given axial pattern is consistent with a certain transverse pattern. The two types of sections will nevertheless be discussed separately since it will be shown that they reveal two different types of superstructures, which are to some extent independent.

In order to emphasize the relationship with the basic perovskite structure with a_p 0.43–0.44 nm all indices refer to this primitive perovskite lattice, which in the present case has a slightly elongated tetragonal unit cell ($c/a = 1$). The direction of the fourfold axis is called $[001]_p$. Sections along the $[110]_p$ and $[100]_p$ zones are called “axial,” where-

as the section along the $[001]_p$ zone axis is called “transverse.”

4.1.2. *Axial sections (along $[hk0]^*$ zones).* Three $[010]_p$ zone patterns are reproduced in Fig. 4. The patterns consist of very strong spots, revealing the basic perovskite lattice, and often, but not always, much weaker spots in rows parallel to $[001]_p$, revealing a superperiod along $[100]_p$. The 000–002 spot distance is divided into a number n of equal intervals with $n = 5$ (Fig. 4c (Ba:Bi = 1:2)), $n = 7$ (Fig. 4a (Ba:Bi = 2:3)), and $n = 9$ (Fig. 4b (Ba:Bi = 4:5)). The corresponding long period along $[001]$ is mostly commensurate, suggesting the presence of a number of $2n$ atomic layers in the superperiod. The 000–002 spot distance is slightly smaller than the 000–200 distance, due to the tetragonal deformation of the average perovskite unit cell in the superstructure. The intensities in the spot rows parallel to $[001]$ show a systematic variation; the spots decrease in intensity with their separation from the intense basic spots such as 002 and 101, as well as with their separation from the

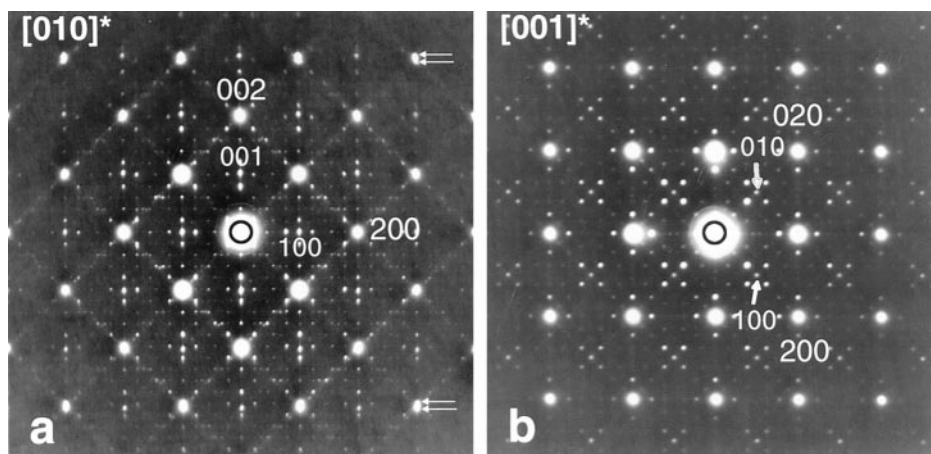


FIG. 5. Composite of two diffraction patterns: (a) along $[010]_p$ zone; (b) along $[001]_p$ zone; One pattern is due to simple perovskite; the second one is due to an island structure.

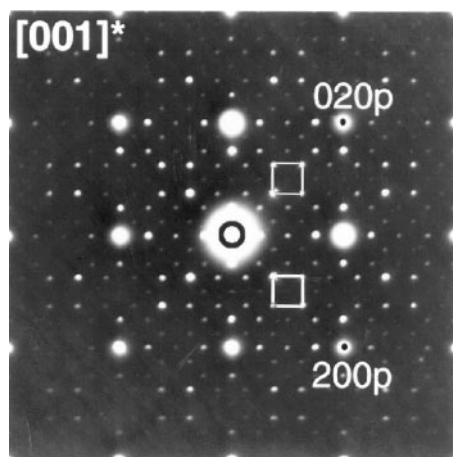


FIG. 6. ED pattern along $[001]_p$ of an area containing a commensurate 4×4 island structure.

positions of potential basic spots such as 001 and 100. In the latter case the spot sequences are shifted over half the interspot distance with respect to the positions of the absent potential basic spots.

The tetragonal deformation is directly evidenced from Fig. 5a, which represents a composite diffraction pattern due to the superposition of a primitive perovskite pattern produced by a region of simple perovskite, adjacent to a region exhibiting the long-period structure with $n = 5$. The spots due to the primitive perovskite, indicated in Fig. 5a, form a square mesh, whereas the corresponding basic spots due to the superstructure form a slightly rectangular arrangement, one side of the rectangle being equally

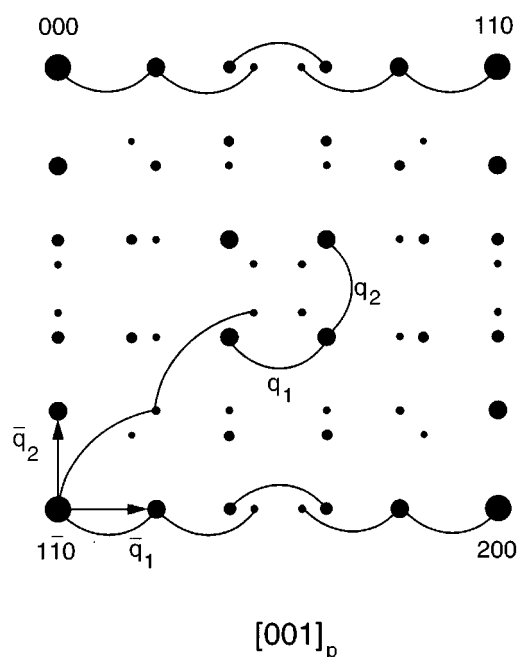


FIG. 8. Schematic representation of the $[001]$ diffraction pattern produced by the island structure of Fig. 9b which consists of 4×4 , 5×5 , and 4×5 islands. The average interfacial spacing in both sets of interfaces is $\frac{2}{9}$. The modulation vectors of both sets are $\mathbf{q}_1 = \frac{2}{9} [110]$ and $\mathbf{q}_2 = \frac{2}{9} [1\bar{1}0]$.

long as the side of the square pattern. This shows directly that the superstructure is based on a somewhat elongated tetragonal unit cell.

Weaker spots in rows perpendicular to the 00l row at the same levels as the spots in the $[001]$ sequences through the

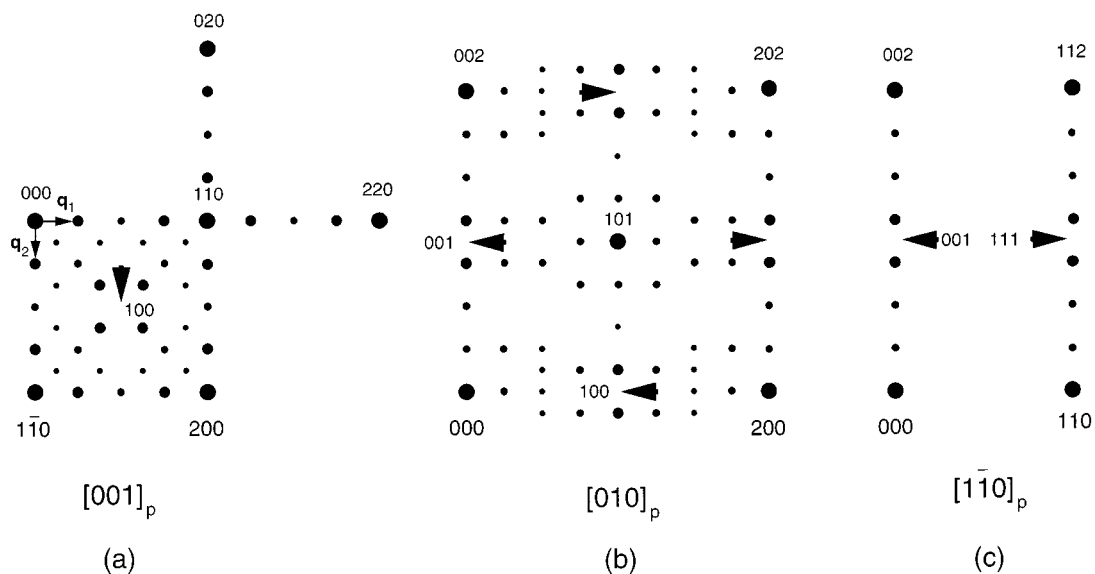


FIG. 7. Schematic representation of diffraction patterns of island fragmented layered perovskite structure of the Ruddlesden-Popper type: (a) $[001]$ pattern; this zone reveals the fragmentation into 4×4 islands. (b) $[010]$ pattern of the 7-layer phase; the perovskite blocks are fragmented into 4×4 islands. (c) $[110]$ pattern of 7-layer compound not exhibiting evidence for island fragmentation.

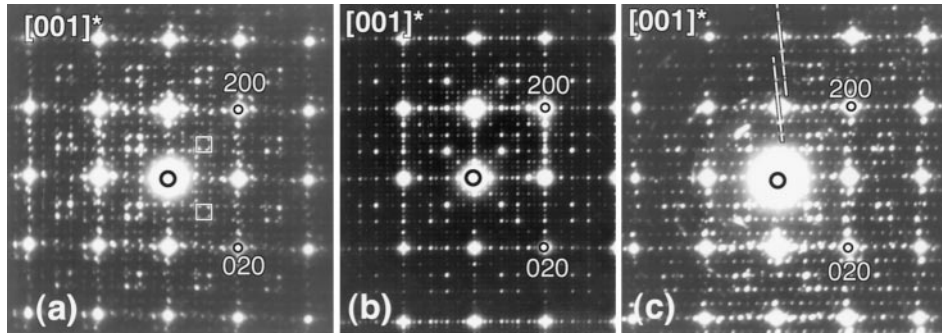


FIG. 9. (a) ED pattern along $[001]^*$ zone exhibiting an orientational anomaly. (b) ED pattern along $[001]^*$ of an area exhibiting the type of HRTEM image shown in Fig. 13. A schematic representation of the ED pattern is shown in Fig. 8. (c) ED pattern along $[001]^*$ of a 5×8 island fragmented structure corresponding to the image of Fig. 14.

basic spots reveal a period within the $(001)^*$ planes. In Fig. 4a (Ba:Bi = 2:3) for instance the 000–200 distance is divided into 10 equal intervals by rows of spots parallel to $[001]^*$. The lattice of nodes within the $(001)^*$ plane is directly revealed in transverse sections along the $[001]^*$ zone.

4.1.3. Transverse zone $[001]^*$. The diffraction patterns along the $[001]^*$ zone (Figs. 6, 7a) show a large diversity in details; they are apparently not directly correlated with the type of superperiod revealed by the axial patterns. In almost all cases the patterns consist of square arrays of relatively very intense spots with $h + k = \text{even}$, revealing the basic perovskite lattice. The spots with $h + k = \text{odd}$ are absent but square clusters of satellite spots are nevertheless associated with these potentially present spots. In Fig. 5b, which is a combined pattern due to a basic perovskite pattern, superposed on a pattern due to a modulated structure, spots with $h + k = \text{odd}$ are actually present as part of the basic perovskite pattern. The combined pattern shows that the $[001]^*$ section of simple perovskite has the same square mesh as that of the superstructure.

In the simplest superstructure one observes the commensurate pattern of Fig. 6 (Ba:Bi = 1:3) represented schematically in Fig. 7a. The 000–110 line segment, i.e., the diffraction vector $[110]^*$ and also the diffraction vector $[1\bar{1}0]^*$, is divided into four equal intervals by satellite spots. The spot positions with $h + k = \text{odd}$ are furthermore the centers of square clusters of satellite spots with the same interspot separation as that in the linear sequences. In fact with each perovskite spot position a square array of satellites can be associated. This square array is unshifted when associated with basic spots for which $h + k = \text{even}$ but is shifted for spot positions with $h + k = \text{odd}$. The intensities of the satellites decrease with increasing separation from the corresponding, either actually present or potentially present, perovskite spot. Commensurate patterns in which the 000–110 segment is divided into five equal intervals are also observed.

Expressed in terms of modulation vectors along the two mutually perpendicular directions one has $\mathbf{q}_1 = \frac{1}{4}[110]$ and $\mathbf{q}_2 = \frac{1}{4}[1\bar{1}0]$ (Fig. 7a) or $\frac{1}{5}[110]$ and $\frac{1}{5}[1\bar{1}0]$. This particular choice of modulation vectors is supported by the observation of incommensurate diffraction patterns such as Fig. 9c (exhibiting a so-called “orientation anomaly”). It is obvious from this figure that unshifted linear sequences of satellites, slightly inclined with respect to the $[110]_p$ and $[1\bar{1}0]_p$ directions, are associated with basic spots for which $h + k = \text{even}$. Such linear spot sequences along parallel directions are also associated with the spot positions for which $h + k = \text{odd}$ but they are now moreover shifted over half of the interspot distance along the two directions parallel to the inclined diffraction vectors.

Next to “orientation anomalies” (Figs 9a, 9c), “spacing anomalies” are also often observed (Figs. 9b (Ba:Bi = 4:11), 10b); they result when the modulation vectors are not simple fractions of either the 110 or the $1\bar{1}0$ diffraction vector. An example is reproduced in Fig. 9b and represented schematically in Fig. 8 for the case where $\mathbf{q}_1 = \frac{2}{9}[110]$ and $\mathbf{q}_2 = \frac{2}{9}[1\bar{1}0]$ with no orientation anomaly present. The resulting patterns still have square symmetry if the length of \mathbf{q}_1 equals that of \mathbf{q}_2 . However, this need not be the case, as the wave vectors \mathbf{q}_1 and \mathbf{q}_2 need not be equal in length; the superstructure is then no longer tetragonal but becomes at most orthorhombic. From the high-resolution images it will become clear that the spacings associated with incommensurate modulation vectors are caused by the presence of a “regular” mixture of two (or more) different spacings in the same parallel sequence of planar interfaces.

More complicated diffraction patterns result if \mathbf{q}_1 and \mathbf{q}_2 not only differ in length but also in orientation. Examples are shown in Fig. 9a and 9c.

4.2. High-Resolution Transmission Electron Microscopy

The presence of several sharp spots in the satellite sequences suggests that the modulations in all three directions,

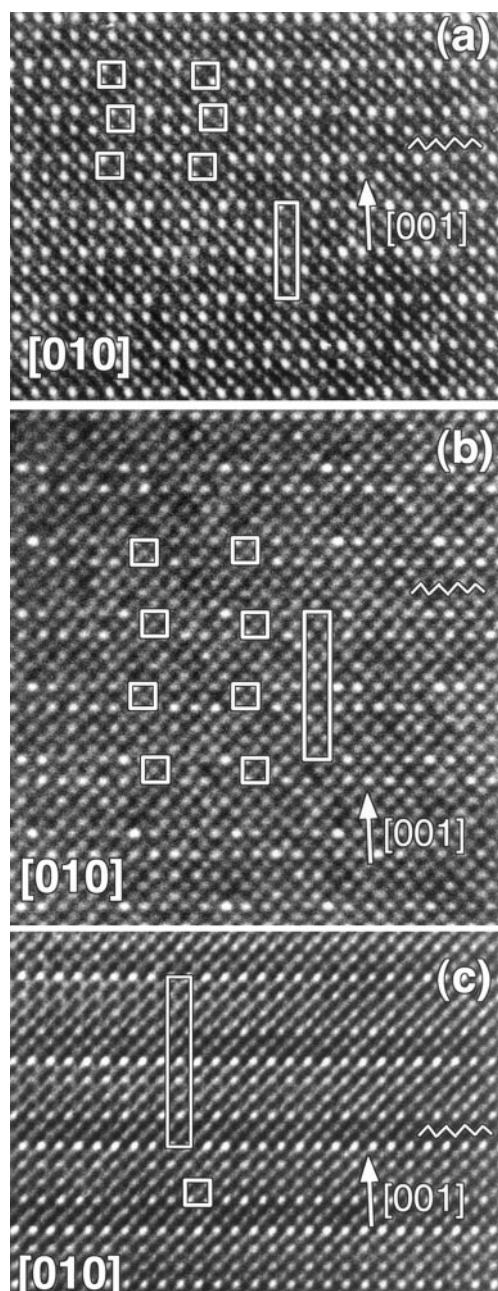


FIG. 10. (a) HREM image along the $[010]$ zone of a 5-layer structure. Note the brightness modulation of the brightest dot rows due to the island fragmentation. (b) HREM image along the $[010]$ zone of a 7 layer structure. Note the brightness modulation of the rows of brightest dots. This suggests that the stacking of the island pattern occurs along a zig-zag sequence. (c) HREM image along the $[010]$ zone of a 9-layer structure.

i.e., along $[001]_p$ as well as along $[110]_p$ and $[1\bar{1}0]_p$, are due to interface modulation, most probably accompanied by composition modulations. Direct imaging by means of HREM is well suited to gain information on the origin of the superstructures especially in the case of

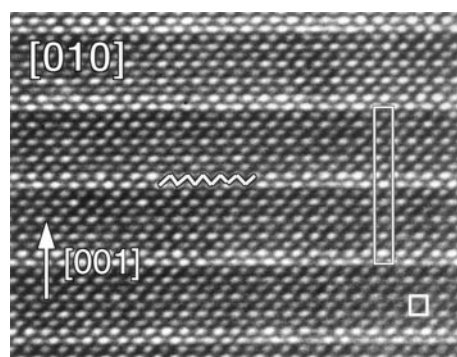


FIG. 11. HREM image of 9-layer structure with ideal composition $Ba_4Bi_5O_y$. The brightest dot rows represent Bi-columns, the less bright dots Ba in this case. Oxygen is not imaged as separate dots. Note the shift over $\frac{1}{2}[111]_p$ along the NaCl type intermediate layer.

interface modulation. In this respect it is important to note that along a cube direction of perovskite different sublattices of heavy atoms are imaged as dots of a different brightness.

4.2.1. *Axial zone images.* Figure 10 shows $[010]$ zone views of the 5-, 7-, and 9-layer superstructures respectively, corresponding with the diffraction patterns of Fig. 4 (Ba:Bi = 1:2, 2:3, 4:5), respectively. The images clearly show lamellae of perovskite unit cells of which the thicknesses are different in the different structural variants. The perovskite lamellae contain respectively two, three, or four layers of unit cells of the basic perovskite, as shown by Figs. 10 and 11 (Ba:Bi = 4:5). The perovskite lamellae are joined by an intermediate layer imaged as a zig-zag line of bright dots as shown in Figs. 10a, 10c. This is caused by an “offset” in such a way that the structures in successive perovskite lamellae are related by a vector of the type $\frac{1}{2}[111]_p$. The configuration of atoms in this intermediate layer must be such that the projection along $[110]$ is consistent with the image of Fig. 12 made along this zone.

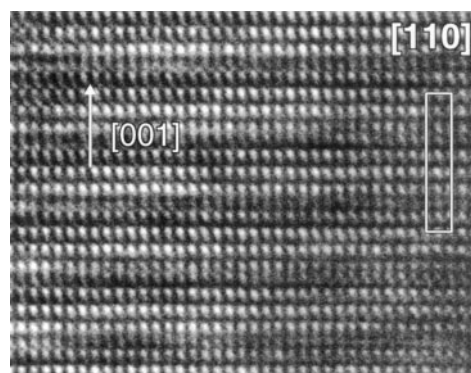


FIG. 12. HREM image along the $[110]$ zone of a 7-layer compound.

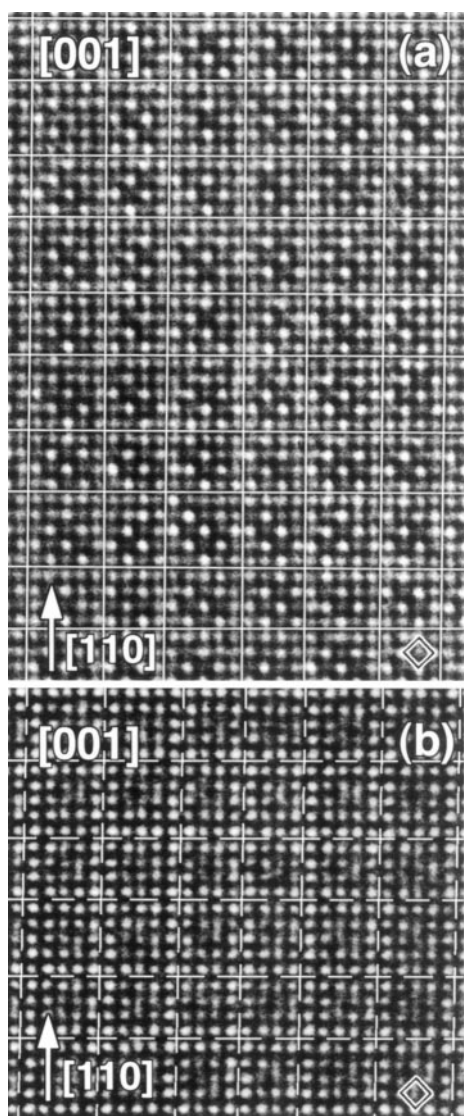


FIG. 13. (a) HREM image along the $[001]$ zone. From the periodic arrangement of bright dots one can deduce that the structure is fragmented in 4×4 , 5×5 , and 4×5 islands. The corresponding diffraction pattern is Fig. 8. (b) $[001]$ HREM image of incommensurate 5×5 structure of the type producing the ED pattern represented schematically in Fig. 8.

From photometer traces parallel to $[001]$ of HREM images across dotted lines parallel to the $[100]$ direction in Figs. 10 and 6 it can be concluded that the interlayer spacing of the heavy atom layers is slightly larger by about 10 to 15% in the intermediate layer than in the perovskite lamellae.

4.2.2. $[001]$ zone images. The images mostly consist of a square grid of bright dots within a mesh of 0.43 nm. Under the appropriate conditions of thickness and defocus the two square sublattices of heavy atom columns are imaged differently. It then becomes evident that the grid consists of small islands of perovskite-like structure (Fig. 13 (Ba:Bi = 4:11)).

Within the islands each dot of one kind has four nearest-neighbors of a different brightness. Along the island edges nearest-neighbor dots of the same brightness occur quasi-systematically, giving rise to a weak darker line. The darkness of the line results in fact from a slightly larger separation of the bright dot rows. The configurations of brightest dots in adjacent islands are thus “out of phase.” All these features are clearly visible in Fig. 13a in which a complex “tartan” structure is present; it consists of 4×4 and 5×5 square islands and of 4×5 rectangular islands in two orientations. The “average” repeat along $[110]_p$ and $[\bar{1}\bar{1}0]_p$ is 4.5 square edges, i.e., $4.5 \times a_p / 2$. Broader dark lines,

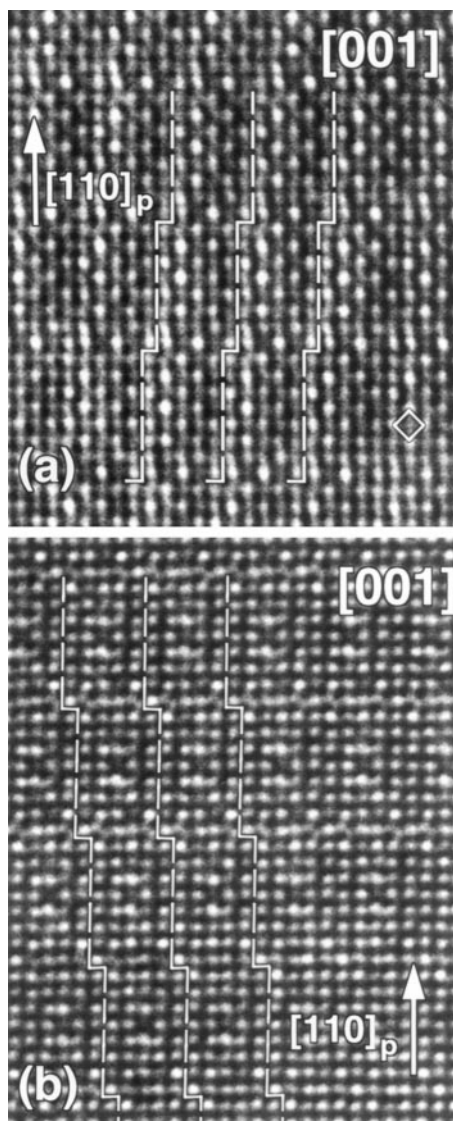


FIG. 14. HRTEM images of a “thick” foil in which the atom columns are imaged as bright dots. Note the presence of 5×8 islands related by a $\frac{1}{2}$ $[110]$ translation. One family of interfaces is systematically ledged which is reflected in the diffraction pattern by the occurrence of orientation anomalies (Fig. 15c).

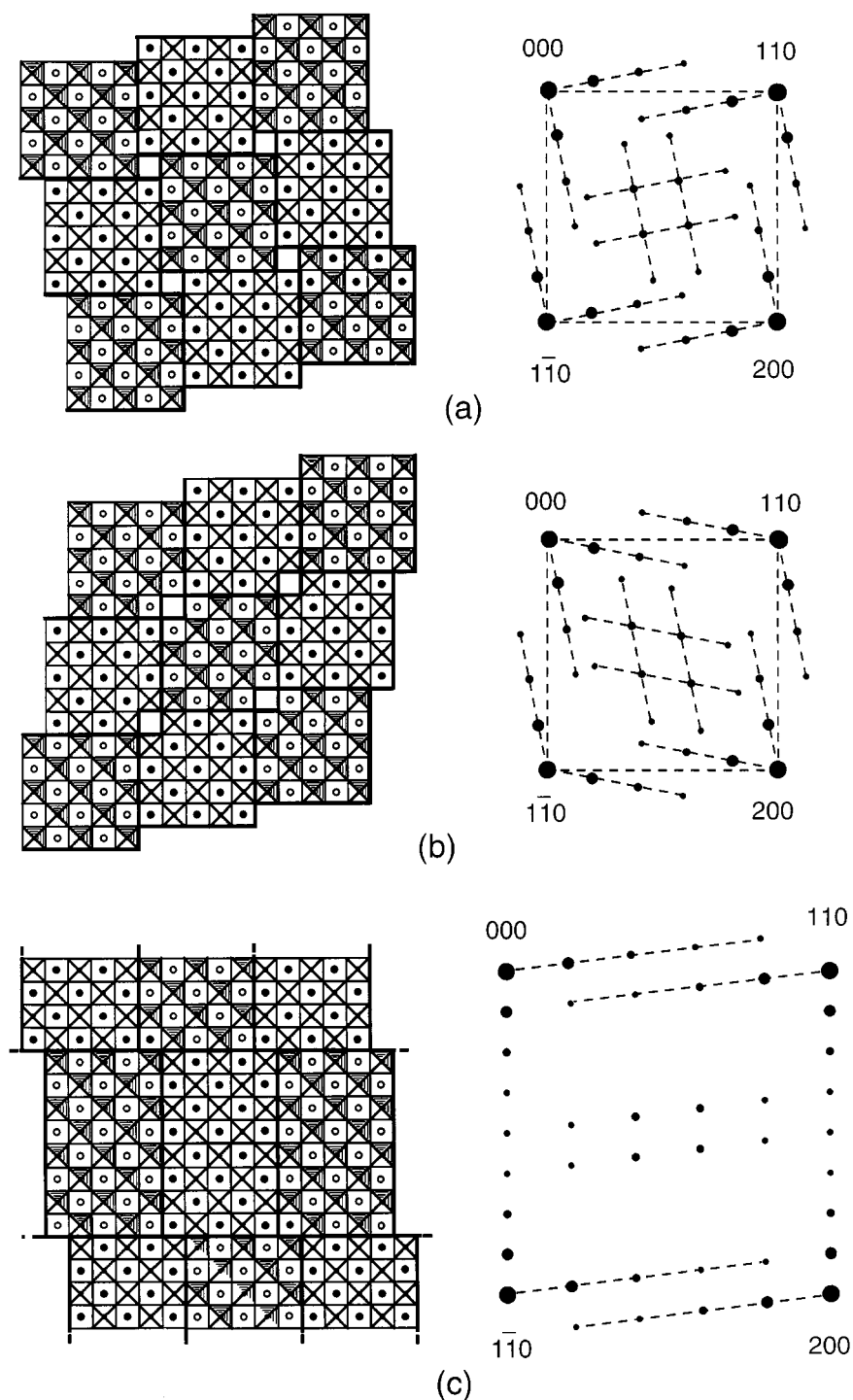


FIG. 15. Different arrangements of 5×5 islands giving rise to orientation anomalies in the corresponding diffraction patterns which are shown schematically. The satellite sequences are connected by dotted lines with the associated basic spots: (a) Fourfold symmetry is conserved. (b) The symmetry is no longer fourfold; only a binary symmetry axis is present. (c) Model of the 5×8 island fragmentation observed in Fig. 14, 25 and of which the corresponding diffraction pattern is shown schematically. Systematic ledging in one set of interfaces causes an "orientation anomaly" in the diffraction pattern.

inclined at 45° with respect to the first set, i.e., parallel to cube directions, pass through the nodepoints of the grid of weak dark lines. The two grids are clearly connected by geometry.

A particularly illustrative image is shown in Fig. 14. It exhibits most of the characteristic features on which the building principle of these structures is based. Successive

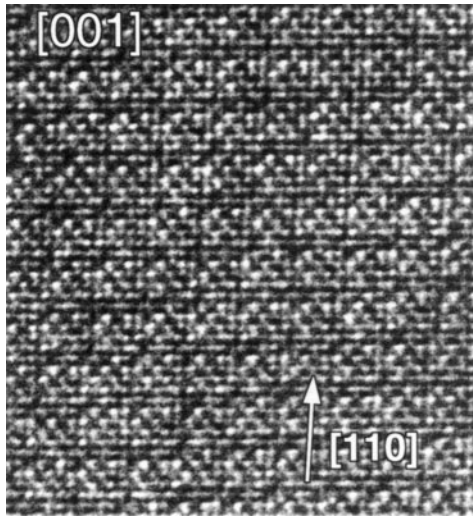


FIG. 16. [001] zone HREM image of incommensurate island structure of the type shown in Fig. 15a,b.

rectangular islands are in this projection systematically shifted over $\frac{1}{2} [1\bar{1}0]_p$ along the $[1\bar{1}0]_p$ direction of the short sides of the rectangles. The resulting two-dimensional lattice is monoclinic. The row of satellites normal to the average direction of the long sides of the rectangles encloses as a result of a small angle α ($\alpha = \arctg \frac{1}{8}$) with the $[110]$ direction as represented schematically in Fig. 15c. The row of satellites perpendicular to the short sides of the rectangles remains parallel to the $[110]$ direction (Fig. 9c). An example illustrating the case represented in Fig. 15a is reproduce in Fig. 16.

5. INTERPRETATION

5.1. Diffraction Patterns

Application of the fractional shift method to the modulated layer structures with $\mathbf{q}_9 = \frac{1}{9} [002]_p$, $\mathbf{q}_7 =$

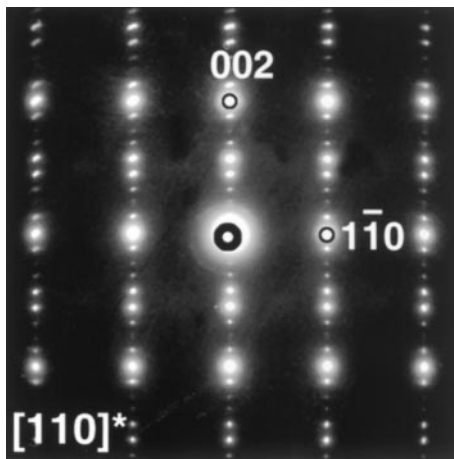


FIG. 17. ED pattern along $[110]_p$ zone of the 9-layer compound.

$\frac{1}{7} [002]_p$, $\mathbf{q}_5 = \frac{1}{5} [002]_p$, and $\mathbf{R} = \frac{1}{2} [111]_p$ leads to a fractional shift of $\frac{1}{2}$ or 0. This can be seen as follows. The fractional shift is in general $\mathbf{h}\cdot\mathbf{R} = \frac{1}{a_p} [hkl] \cdot (\frac{1}{2}) a_p [111] = \frac{1}{2} (h+k+l)$. For the $[010]_p$ zone this becomes $\mathbf{h}\cdot\mathbf{R} = \frac{1}{2} (h+k)$, i.e., $\frac{1}{2} \pmod{1}$ if $h+k = \text{odd}$ and $0 \pmod{1}$ if $h+k = \text{even}$.

In the $[1\bar{1}0]$ zone pattern the fractional shift is $\frac{1}{2} l \pmod{1}$ since $h+k = \text{even}$, i.e., $\mathbf{h}\cdot\mathbf{R} = 0 \pmod{1}$ if $l = \text{even}$ and $\frac{1}{2} \pmod{1}$ if $l = \text{odd}$ (Fig. 7c). It is obvious from Fig. 17 that this is in accordance with the observed fractional shifts.

The modulation vectors describing the island structure are $\mathbf{q}_1 = \frac{1}{n} [110]$ and $\mathbf{q}_2 = \frac{1}{m} [1\bar{1}0]$ with $n = m = 4$ in the simplest case of square islands. However $n = m = 5$ also occurs as well as fractional values resulting from mixtures of 4 and 5 such as for $n = m = \frac{2}{5}$. More complicated situations arise in cases where the islands are rectangular, e.g., $n = 5$, $m = 8$. The projected displacement vectors are $\mathbf{R}_1 = \frac{1}{2} [110]_p$ and $\mathbf{R}_2 = \frac{1}{2} [1\bar{1}0]_p$. This leads in the $[001]_p$ zone to fractional shifts given by $\mathbf{h}\cdot\mathbf{R} = \frac{1}{2} (h+k)$, i.e., $\frac{1}{2} \pmod{1}$ for reflections with $h+k = \text{odd}$ and $0 \pmod{1}$ for reflections with $h+k = \text{even}$ (Figs. 15a, 15b).

The two-dimensional character of the modulated structure leads to the formation of arrays of superstructure spots associated with each of the basic spots. These arrays are shifted fractionally along two directions simultaneously; over $\mathbf{h}\cdot\mathbf{R}_1$ along $[110]$ and over $\mathbf{h}\cdot\mathbf{R}_2$ along $[1\bar{1}0]$. These features are clearly exhibited in the patterns of Figs 6 and 7a.

The particular choice of modulation vectors is supported by the observation of incommensurate diffraction patterns such as those of Figs. 9a and 9c, exhibiting a so-called orientation anomaly. It is obvious from this figure that unshifted linear sequences of satellites, slightly inclined with respect to the $[110]_p$ and $[1\bar{1}0]_p$ directions, are associated with basic spots for which $h+k = \text{even}$. Such linear sequences along parallel directions are also associated with

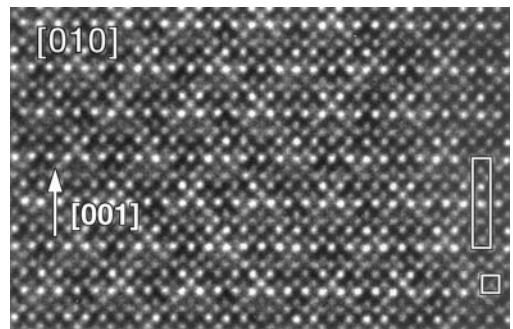


FIG. 18. $[010]_p$ HREM image of a 5-layered compound with ideal composition $\text{Ba}_2\text{Bi}_3\text{O}_y$. The 5-layer period is evident from extra bright dot rows perpendicular to $[001]$. Note also the prominent bright lines of dots under $\approx 45^\circ$ with the $[001]$ direction resulting from a fourfold period within the layer planes.

the spot positions $h + k = \text{odd}$ but they are now moreover shifted over half of the interspot distance along the two directions parallel to the inclined diffraction vectors.

The fractional shifts observed in the $[001]_p$ zone ED pattern do not make it possible to deduce a possible component along $[001]_p$ of the displacement vectors \mathbf{R}_1 and \mathbf{R}_2 of the island boundaries. We shall see below that the $[010]$ HREM images discussed are consistent with \mathbf{R}_1 and \mathbf{R}_2 vectors of the type $\frac{1}{2}[111]$, i.e., of the same type as the displacement vector associated with the $[001]$ intermediate layer.

Next to orientation anomalies, spacing anomalies are also often observed; they result when the modulation vectors are not simple fractions of either the 110 or the $1\bar{1}0$ diffraction vectors. An example is reproduced in Fig. 9b and represented schematically in Fig. 8 for the case where $\mathbf{q}_1 = \frac{2}{9}[110]$ and $\mathbf{q}_2 = \frac{2}{9}[1\bar{1}0]$ with no orientation anomaly present. The resulting patterns still have square symmetry if the length of \mathbf{q}_1 equals the length of \mathbf{q}_2 . However this need not be the case as the wave vectors \mathbf{q}_1 and \mathbf{q}_2 need not be equal in length; the superstructure is then no longer tetragonal but becomes at most orthorhombic. From the high-resolution images it will become clear that the spacing associated with incommensurate modulation vectors are caused by the presence of a “regular” mixture of two (or more) different spacings in the same parallel sequence of planar interfaces.

5.2. HREM Images

5.2.1. Axial zone images. The high resolution image of Fig. 18 (Ba:Bi = 1:2) refers to a 5- (10-) layered structure viewed along $[010]$. The five-layer period along $[001]$ is obvious from the separation of the dense rows of extra bright dots and is confirmed by the $[00\bar{l}]$ row of spots in the corresponding ED pattern of Fig. 4c. This image and the corresponding diffraction pattern also confirm the small tetragonal deformation along $[001]$ ($c/a = 1$). One of the parallel layer lines of bright dots exhibits a varying brightness with a fourfold period. This is a strong indication that the perovskite blocks are fragmented into 4×4 islands. The corresponding $[010]$ diffraction pattern of Fig. 4c exhibits orientation anomalies in the satellite sequences associated with the basic spots and which enclose a small angle with the $[011]$ and $[0\bar{1}1]$ directions. These rows of satellite reflections reveal an incommensurate quasi-fourfold period. A detailed analysis of Fig. 18 and of the corresponding ED pattern is given below in Section 6.2.

5.2.2. Transverse images. The $[001]$ zone images exhibit usually “tartan” patterns of bright (or dark) lines parallel to $[110]_p$ and $[1\bar{1}0]_p$ that are due to the traces of interfaces separating the islands. In some cases rows of extra bright dots along the $[100]_p$ and $[010]_p$ directions also become

visible as in Figs. 13 and 14. These lines result from the interference between the beams that produce the square of rather intense diffraction spots around the 100 -type nodes (Fig. 7a). The actual boundary images are produced by the interference of beams corresponding with the linear arrays of satellites along $[110]_p$ and $[1\bar{1}0]_p$ with modulation vectors \mathbf{q}_1 and \mathbf{q}_2 respectively. The interference between beams corresponding to diagonally related intense spots of the square produce such parallel “ghost” lines with a spacing corresponding to a modulation vector $\mathbf{q}_1 + \mathbf{q}_2$. Some caution is therefore needed when associating lines of singular dots (extra bright or extra weak) with the traces of interfaces.

5.2.3. Lattice relaxation along boundaries. From diffraction patterns such as those in Figs. 5a and 5b, it was deduced that the primitive perovskite subcell, which is prominently revealed by the most intense spots in patterns produced by the layered superstructure, is slightly tetragonally (perhaps orthorhombically) deformed such that $a = a_p$ but $c = a_p$. The effective c/a ratio is found to depend on the number of layers in the unit cell; it is 1.012 in the 9-layer compound, 1.032 in the 7-layer compound, and 1.045 in the 5-layer compound. This is consistent with the assumption that the NaCl-like configuration in the intermediate lamellae causes a slight local expansion.

In order to localize unambiguously the origin of this expansion along c , photometer traces were obtained from digitized high-resolution images such as Fig. 10c. The intensities of the spots along the layer lines were first averaged; subsequently, the intensity of the one-dimensional profile so obtained was determined and a print-out of the intensity trace was made. From this trace it can be concluded that the interlayer spacing in the intermediate lamellae is about 10 to 15% larger than that within the perovskite blocks. Computing the average interlayer spacing in terms of a_p leads to the c/a_p ratios observed for the three examined layered compounds. These c/a_p ratios are “local” values that cannot be compared directly with the average values obtained by X-ray

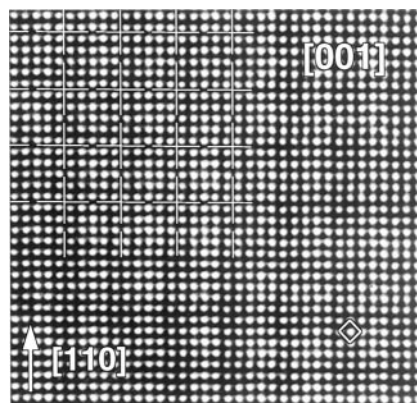


FIG. 19. HREM image along $[001]_p$ of 5×5 island structure.

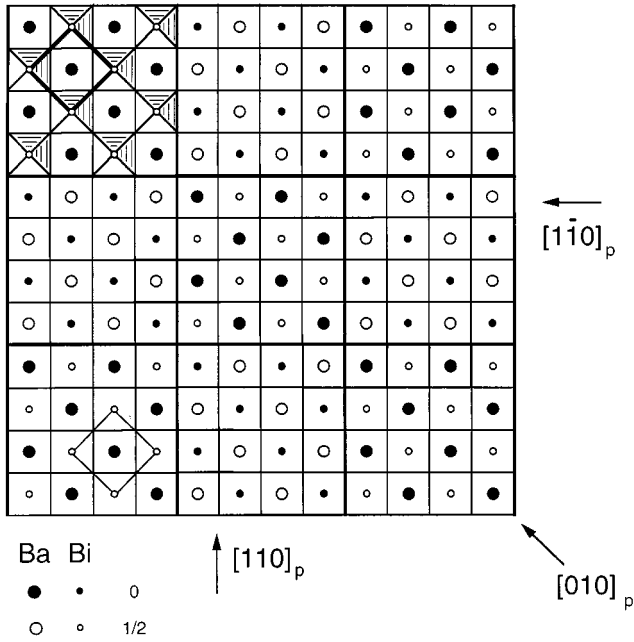


FIG. 20. $[001]$ view of a perovskite lamella of the checkerboard 4×4 island fragmented structure. It contains the perovskite structure at two different levels along the $[001]_p$ direction. The 5-layer 4×4 island fragmented R-P phase is based on the stacking of such lamellae alternating with NaCl-like layers.

diffraction mentioned in Table 1; however, both vary in the same sense, i.e., decrease with the number of layers.

A different type of local lattice relaxation is to be expected along the island boundaries or “shear planes” since along such interfaces the configuration of nearest-neighbor atoms differs from that within the islands, where the normal perovskite configuration prevails. Photometric traces were made along lines perpendicular to intensity-averaged dot rows parallel to such interfaces in the island structure of Fig. 14. The limiting bright dot rows adjacent to the boundaries between two islands are found to be about 4–5% more widely separated than the bright dot rows within the islands.

6. STRUCTURAL MODELS

6.1. Layer-Like Stackings: Unfragmented Structures

The HREM observations suggest possible structure models for the basic layer structures. The difference in the number of layers in the unit cell along $[001]$ as observed in the simplest $[010]_p$ high-resolution images such as Figs. 10a and 11 can be rationalized by assuming the existence of idealized layer-like structures with ideal compositions $\text{Ba}_4\text{Bi}_5\text{O}_y$, $\text{Ba}_3\text{Bi}_4\text{O}_y$, and $\text{Ba}_2\text{Bi}_3\text{O}_y$, corresponding respectively to the structures with 9, 7, and 5 atomic layers in the repeat unit, i.e., 18, 14, and 10 atomic layers in the unit cell along $[001]$. These idealized long-period superstructures have a tetragonal body-centered lattice. The displacement vector $\frac{1}{2}[111]_p$ connecting two successive perovskite lamellae

also causes the average unit cell of the perovskite substructure to be body centered, which is reflected in the diffraction patterns by the absence of basic reflections for which $h + k = \text{odd}$. This can be understood from the fact that the $\frac{1}{2}[111]_p$ displacement, when applied to the perovskite structure, effectively interchanges Ba and Bi sites.

The commonly known perovskite-like intergrowth structures were considered when deriving a possible structure of the intermediate layer between $\frac{1}{2}[111]_p$ displaced successive perovskite lamellae. Three different types of models are compatible with the general features of the high-resolution images of the intermediate layer and with the diffraction patterns.

The formation of a body-centered unit cell can be achieved if two AO atomic layers are placed between the perovskite lamellae. These layers form a $-AO-OA-$ stacking sequence and can be formally described as the rocksalt-type structure. If the perovskite blocks are terminated by BO_2 layers, the resulting structure is similar to the homologue series of the Ruddlesden–Popper (R–P) phases $A_{n+1}B_nO_{3n+1}$ where n describes the thickness of the perovskite block (model I) (Fig. 2c). The structure prototype with perovskite blocks terminated by AO layers can be found in Bi-containing superconductors $\text{Bi}_2\text{Sr}_2\text{Ca}_{n-1}\text{Cu}_n\text{O}_{2n+4+\delta}$ (model II) (Fig. 2a). The third possibility is realized in Aurivillius-like phases $A_{n+1}B_nO_{3n+3}$ where $-AO-O_2-OA-$ blocks are placed between the perovskite lamellae terminated by BO_2 layers (model III) (Fig. 2b).

We must assume that the formation of the intergrowth structures allows the material to accept an excess of Bi, which is probably concentrated in the layers between adjacent perovskite lamellae. The cation positions in the intermediate layers for the compounds investigated are occupied preferentially by Bi, but the mixed occupation of these positions by Bi and Ba also cannot be excluded.

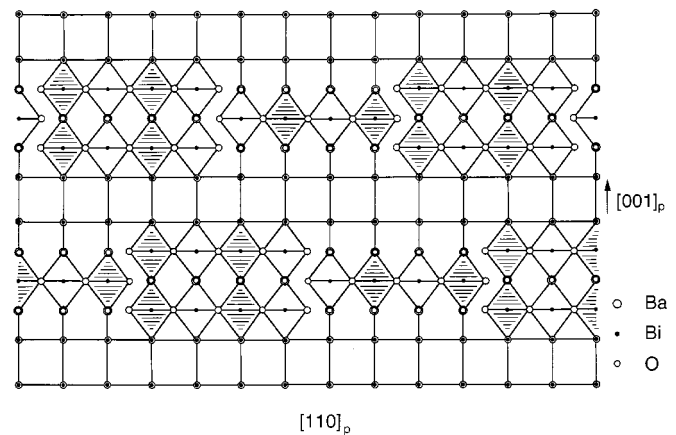


FIG. 21. Cross-sectional view along $[110]_p$ of the 5-layer R-P like phase based on the island fragmented lamellae of Fig. 20. This model is consistent with the incommensurate ED pattern of Fig. 4c.

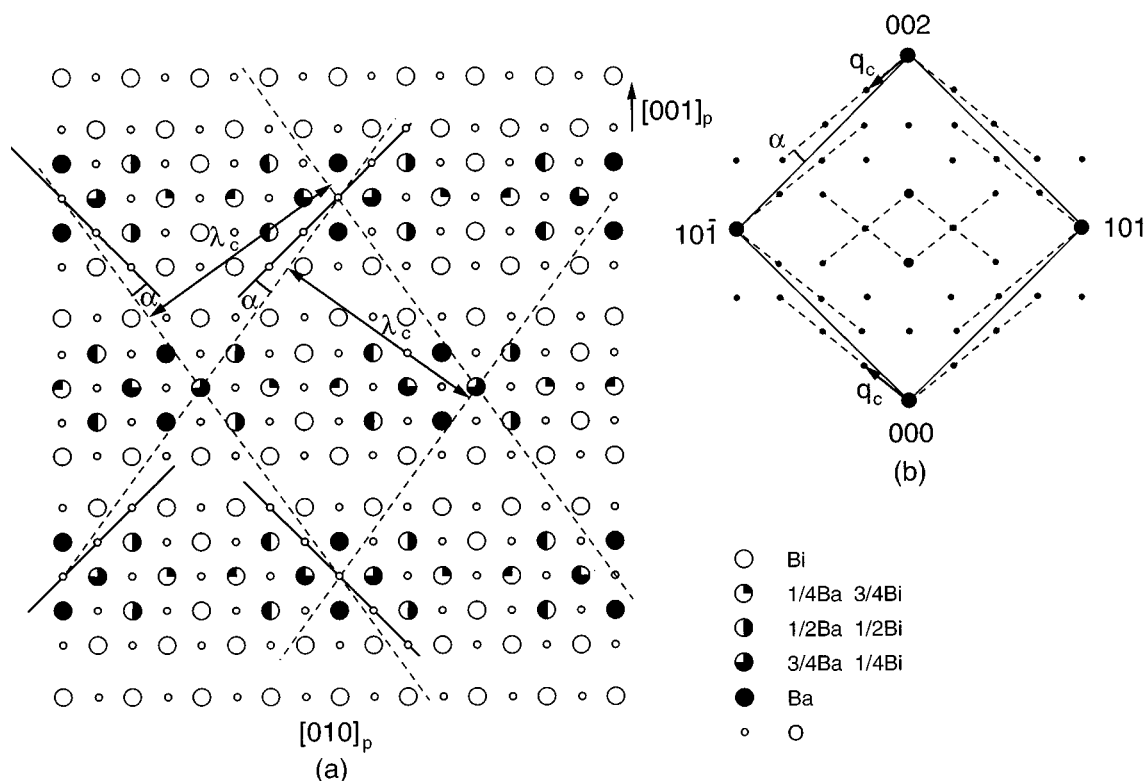


FIG. 22. (a) Projected view along $[010]_p$ of the 5-layer 4×4 island fragmented R–P-like phase. The lattice of the pattern of columns is based on a centred square with size $a_p \times a_p$. Note in particular the 4-fold period along $[100]_p$ of the occupation of the columns which is represented by partly shaded circular disks. This gives rise to occupation waves with incommensurate wavelength λ_c of which the wave fronts enclose a small angle with the $[101]$ direction. (b) Schematic representation of incommensurate $[010]_p$ zone diffraction pattern corresponding to (a) and observed in Fig. 4c.

All proposed models produce a $\frac{1}{2}a[111]_p$ shift between perovskite blocks and the same configuration of heavy ion columns in the projected structure along $[010]_p$. However, we found that the presence of additional oxygen atoms between two AO layers in the Aurivillius-type structure produces significant differences between experimental and calculated images, and model III was thus rejected.

A distinction between models I and II (Fig. 2) comprising the rocksalt intermediate layers is not obvious. Indeed, the HREM images, calculated using these models, show good agreement with those observed experimentally at several values of the defocus values and thicknesses. A discussion of the interatomic distances might therefore be useful to estimate the probability of the existence of those two structures.

The Bi–O distances in the intermediate layer of the rocksalt-type structure can be easily calculated using the matching requirement with neighboring perovskite blocks with a known subcell dimension of 4.3 Å. Since $a_{\text{NaCl}} = \sqrt{2}a_{\text{per}}$, the Bi–O separation within BiO layers should be as large as $d_{\text{Bi-O}} = 4.3 \times 2/\sqrt{2} = 3.04$ Å. The observed separation between Bi-containing layers as deduced from the zig-zag configuration of bright dots in images such as Figs. 10a and 10c is found to be about 2.15–2.2 Å.

In model I the Bi cations are surrounded by four oxygens within the BiO layer plane with $d_{\text{Bi-O}} = 3.04$ Å, four oxygens from the neighboring BiO₂ layer with $d_{\text{Bi-O}} = 3.07$ Å, and one oxygen from the BiO layer with $d_{\text{Bi-O}} = 2.2$ Å, giving an average Bi–O distance of 2.96 Å.

In model II, Bi cations are situated in apically compressed octahedra with equatorial bonds of 3.04 Å and apical ones of 2.15 Å (the average distance is equal to 2.74 Å). Such bond lengths seem to be too long even for Bi³⁺ cations if we compare them to the distance in Bi₂O₃, which does not exceed 2.319 Å. Nevertheless, BiFeO₃ and (K_{0.87}Bi_{0.13})BiO₃ perovskites, where Bi³⁺ cations occupy 12-coordinated positions in the A sublattice with a Bi–O distance as long as 2.79–2.994 Å, are known. The partial occupation of the cation positions in the intermediate layers by Ba and Bi is also a possible explanation for unusually long interatomic distances. We must conclude that the comparison of the interatomic distances does not make it possible to choose unambiguously between models I and II, and both of them can be accepted with equal probability on this basis.

The general composition for model I is expressed by the formula $\text{Ba}_n\text{Bi}_{n+3}\text{O}_{3n+4}$ and the compound with $n = 1$

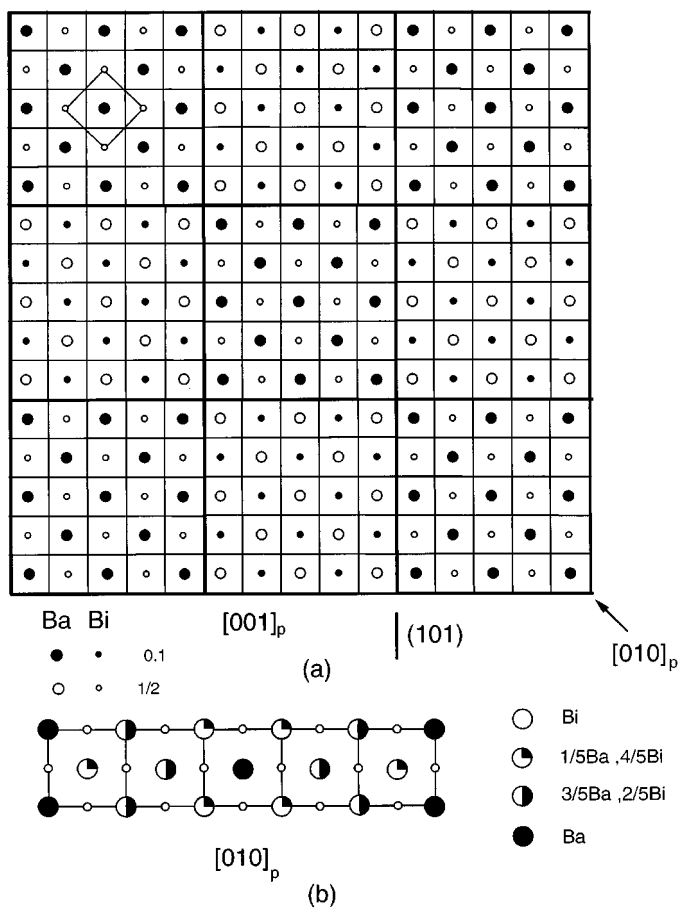


FIG. 23. (a) [001] view of a perovskite lamella of the 5×5 island structure. It contains the perovskite structure at two different levels along the $[001]_p$ direction. The 5×5 island fragmented 7-layer R-P-like phase is based on the stacking of such lamellae. (b) One period of the $[010]$ view of the occupation of the lattice of $[010]$ columns.

should contain only Bi^{3+} cations. The formal oxidation state of Bi approaches $+4$ with $n \rightarrow \infty$ for BaBiO_3 . The partial replacement of Bi cations by Ba ones in BiO layers will lead to an increase of the Bi formal valence in comparison with that of the ideal composition. For example, the compound with $n = 1$ and the 50%Bi + 50%Ba occupation of the positions in the intermediate layers will lead to the $\text{Ba}_2\text{Bi}_3\text{O}_7$ composition and $V_{\text{Bi}} = +3.33$. Thus model I makes it possible to vary the cation ratio over a wide range and also provides the possibility of forming anion-deficient structures to diminish the formal Bi valence. It will be shown below that the anion deficiency can possibly be accommodated by the formation of island structures.

The Bi oxidation state imposes restrictions on the possible cation compositions for the $\text{Ba}_n\text{Bi}_{n+1}\text{O}_{3n}$ compounds corresponding to model II. Since the lowest possible oxidation state of Bi is $+3$, the compounds with $n = 1, 2$ are presumably not stable. The third member of this series $\text{Ba}_3\text{Bi}_4\text{O}_9$ exhibits $V_{\text{Bi}} = +3$ and, consequently, no anion

deficiency and replacement of Bi by Ba can be realized for this compound. Hence, on this basis the idealized model II can be accepted only as a possible structure of the compounds when the number of layers per body-centered unit cell is equal to or larger than 18 (9-layer compound). We suggest that both models I and II can be present in the island fragmented structures.

6.2. Island Fragmented Structure of Perovskite Lamellae

Deviations from the simple compositions mentioned above can be further accommodated by the formation of planar defects, as suggested by Fig. 1.

The image of Fig. 14 was made along the $[001]$ zone. It exhibits a tiling of rectangular perovskite islands limited by $(110)_p$ and $(\bar{1}10)_p$ planes. Each island is imaged by a two-dimensional array of 8 by 5 bright dots of two brightness classes, forming centered squares. The structure is schematically represented as a checkerboard pattern of BiO_6 octahedra and BaO_4 squares as in the perovskite structure (Fig. 15c). Ba columns and BiO mixed columns are imaged differently under the imaging conditions prevailing in Fig. 14, the perovskite structure being imaged along this zone as a square of equally bright dots centered by a dot of different brightness. Using this imaging code it is possible to deduce the relative positions of the perovskite structures in adjacent islands. In particular it is thus also possible to find the configuration of columns along the interface, assimilating dots of the same brightness with columns consisting of atoms of the same chemical species. By this procedure one finds that almost systematically pairs of columns with the same brightness face one another in adjacent sites across the boundary. This suggests that columns of the same nature are close neighbors along the boundaries of the islands.

Due to the relative displacement over $\frac{1}{2}[111]$ of successive perovskite blocks, all $[001]$ columns within the layered structures become mixed columns containing, apart from oxygen, bismuth and barium, ideally in equal numbers. Column contrast is therefore likely to be small along $[001]$; it will be optimum for a specimen thickness equal to a half integral number of unit cells since then one atomic species predominates in each column. Moreover the resulting contrast will be the stronger the thinner the foil, i.e., the smaller the number of unit cells along the column.

Assuming the layered structure to be also island fragmented these contrast considerations still apply to each island. In fact from observations on wedge-shaped samples we concluded that in the $[001]$ view the thickness is a crucial parameter for optimum column contrast. In most cases the $[001]$ column contrast is small even under adequate diffraction conditions because the atomic scattering factors of Ba and Bi do not differ very much.

Taking into account these limitations it is still justified to assume that if column contrast is present in the $[001]$ zone

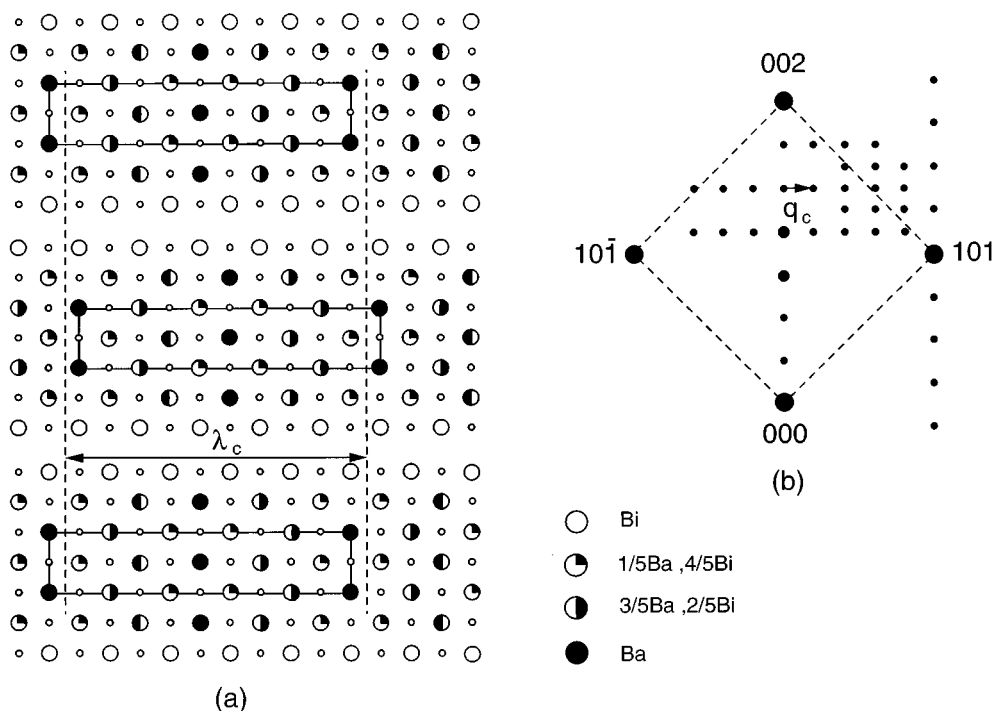


FIG. 24. (a) Projected view along $[010]_p$ of the 7-layer 5×5 island fragmented R–P-like phase. The periodic occupation of the columns is indicated schematically by partly shaded disks; note the commensurate wavelength $\lambda_c = 5a_p$ of the occupation waves. (b) The $[010]_p$ zone commensurate ED pattern corresponding to (a) and Fig. 4a.

image it must be attributed to columns with different heavy atoms and hence can be used to relate the structures in adjacent islands.

The simplest island fragmentation model, consistent with images such as Figs. 13 and 19 and assuming that columns with the same cation occupation are in adjacent positions along the $\{110\}$ boundaries, is represented in Fig. 20. We call it the 4×4 island model. The first question to be settled is whether the displacement vectors have a component along $[001]$, i.e., whether the displacement vectors \mathbf{R}_1 and \mathbf{R}_2 are of the type $\frac{1}{2}\langle 110 \rangle_p$ or $\frac{1}{2}\langle 111 \rangle_p$. In the latter case the differently shaded circular dots in Fig. 21 correspond to Ba and Bi ions at levels differing by $\frac{1}{2}[001]_p$. The $[001]_p$ HREM images are not visibly influenced by this level difference since the heavy atom column compositions along $[001]_p$ remain the same. However the column geometry of the island fragmented structure, as viewed along $[010]_p$ depends on the displacement vectors; thus its study makes it possible to settle this question.

We consider in particular the idealized 5-layer 4×4 island fragmented superstructure of which the $[001]_p$ projection is shown in Fig. 20. Assuming displacement vectors of the type $\frac{1}{2}[111]$ for the island boundaries a view along $[110]_p$ where the island boundaries are seen edge on is represented in Fig. 21. In the idealized model they contain a local excess of oxygen ions, forming a single layer on a rectangular pattern.

Half of the islands forming the checkerboard pattern of Fig. 20 contain a R–P-like structure (model I); the other half have the “alternative R–P-like structure” (model II). The sodium chloride-like lamella of BiO is continuous across the island boundaries. This is geometrically possible because the displacement vector $\frac{1}{2}[111]_p$ is a lattice vector of the sodium chloride-type layer.

The $[010]_p$ view is the most informative one since the heavy atom column geometry along this direction depends on the type of displacement vector of the island boundaries. In the absence of a $\frac{1}{2}[001]_p$ component the $[010]_p$ the heavy atom columns project on a primitive square pattern with a mesh size of $\frac{1}{2}a_p$, whereas the observed pattern exhibits a centered square mesh with a size a_p . This $[010]_p$ projection is shown in Fig. 22a. This remark suggests the presence of a $\frac{1}{2}[001]$ component such as shown in the model of Fig. 21. In the $[010]_p$ projection of Fig. 22a we have represented the composition of each column, demonstrating the fourfold period along the layer lines. The “phase” of the periodic composition modulation as observed in a HREM image along $[010]$ allows us to deduce the relative positions of successive perovskite blocks. The HREM image of Fig. 18 suggests the structure model indicated in Figs. 21 and 22a.

We now demonstrate that this model is also consistent with all details of the ED pattern along $[010]_p$ of Fig. 4c and is represented in Fig. 22b. This pattern is incommensurate. The rows of satellite spots associated with all the basic spots

of the five-layered structure enclose a small angle α (Fig. 4c) with the $[101]$ direction, and moreover the satellite separation is slightly smaller than one-quarter of the $000-101$ distance. This leads to rows of superstructure spots, which are not exactly aligned along $[001]$; they form a zig-zag line. The superstructure spots remain aligned along $[100]$ but along this direction they exhibit a spacing anomaly. There are no fractional shifts along the satellite rows. All these detailed features can be understood on the basis of the projected structure model of Fig. 22. This model demonstrates that the 4×4 island fragmented 5-layered structure is composition modulated, the composition wave fronts having the direction and wavelength indicated in Fig. 22a. Also the $[101]$ direction is indicated; it clearly encloses the same small angle α with the direction of the composition wave fronts. Moreover the wavelength λ_c is somewhat larger than four times the meshsize of the square pattern. A second set of concentration waves is symmetry related to this first set by a mirror operation with respect to the $[001]$ line. The absence of fractional shifts is consistent with the suggested composition modulation [17] in contrast with interface modulation.

The same type of reasoning will now be applied to the 7-layered 5×5 island fragmented structure of which the $[010]_p$ ED pattern is shown in Figs. 4a and 7b and the HREM image in Fig. 10b. The $[001]$ projection of the perovskite lamella of the 5×5 island fragmented superstructure is represented in Fig. 23a, assuming the presence of a $\frac{1}{2}[001]$ component for the displacement vector of the island boundaries. The fact that the island size is now an odd number of elementary cube edges long changes the resulting stacking of lamellae rather profoundly as compared to the 4×4 case, as will now be demonstrated. Figure 23a shows the $[001]$ projection; only heavy atom columns are indicated. The corresponding $[010]_p$ view exhibiting the fivefold period is indicated in Figs. 23b and 24a. A unit mesh ($7a_p \times 5a_p$) for the lamellae stacking can now be adopted and is represented in Fig. 24a. The lattice of the composition distribution is thus commensurate with the lattice of the ideal 7-layered structure. The primary composition wave fronts are now parallel to $(100)_p$ planes, the wavelength being $5a_p$. The ED pattern (Figs. 4a, 24b) thus exhibits satellite spot sequences parallel to $[100]_p$ centered on the basic 7-layered structure spots and with a \mathbf{q} vector $\frac{1}{5}[100]_p$. There are clearly no fractional shifts parallel to $[100]$. Successive satellite rows are interleaved along the central line parallel to $[001]^*$ midway between two rows of intense 7-layered structure spots, proving their relation to this structure. The interleaving of the satellite sequences is clearly a consequence of the fractional shifts of the $h0l$ ($h = \text{constant}$) rows of the basic 7-layer structure spots associated with $h + l = \text{odd}$ node positions.

In the ideal 5×5 island model of Fig. 23a the “corners” of the islands are all occupied by Ba columns, leading to an

excess of Ba in the perovskite block. An alternative structure can be envisaged in which the corner columns are all occupied by Bi, leading likewise to an excess of Bi in the perovskite block. In the 4×4 island model the perovskite block has the macroscopic perovskite heavy atom concentration ratio irrespective of the occupation of the corner columns. The island size is thus composition dependent. Layer sequence, perovskite block size, and island size are thus structural features that make it possible to accommodate a wide range of compositions. The oxygen layer along the island boundaries may further contribute to adjust the oxygen contents by the formation of vacancies in this layer.

The discussion on the relative stability of models I and II for the unfragmented structures has shown that arguments supporting one phase over the other were difficult to find on the basis of crystal chemical considerations. It turns out that in the island fragmented structures blocks of both phases occur in equal volumes. This, in a sense, is a manifestation of the almost equal stability of both phases.

6.3. Origin of Orientation and (or) Spacing Anomaly

The diffraction patterns of Figs. 8 and 9b corresponding with the high-resolution image of Fig. 13a reveal spacing anomalies, but no orientation anomalies. From the high-resolution image it is evident that the corresponding structure is fragmented into square and rectangular islands of dots limited by interfaces parallel to (110) and $(1\bar{1}0)$ traces. The separation of the interfaces is similar in the two mutually perpendicular sets of parallel interfaces; it consists of an ordered mixture of bands of 4 and 5 unit squares (Fig. 13a), i.e., squares of $(\frac{a_p}{2}) \times (\frac{a_p}{2})$. The average separation is thus 4.5 unit squares in both sets. The modulation vectors are thus $\mathbf{q}_1 = \frac{2}{5}[110]_p$ and $\mathbf{q}_2 = \frac{2}{5}[1\bar{1}0]_p$. The intersection of the two sets of parallel interfaces generates a “tartan” pattern of squares and rectangles.

In the diffraction pattern (Figs. 8, 9b) satellite sequences at $m\mathbf{q}_1$ and $n\mathbf{q}_2$ (m, n integers) originate from basic spots with $h + k = \text{even}$. Moreover similar satellite arrays are associated with spots with $h + k = \text{odd}$ but these are fractionally shifted over $\frac{1}{2}$. It turns out that, moreover, arrays of satellite spots must be associated with virtual spots (e.g., $\frac{1}{2} \frac{1}{2} 0$) with half-integral indices with respect to the lattice $a_p^* \times a_p^*$. Such positions correspond to diffraction vectors $\frac{1}{2}[110]_p$ and $\frac{1}{2}[1\bar{1}0]_p$, and they have fractional shifts of $\pm \frac{1}{2}$ associated with them. This feature suggests that the “basic” structure, i.e., the structure within the islands, may have a superstructure with unit mesh $2a_p \times 2a_p$.

The HREM images along the $[001]_p$ zone axis are complicated by the fact that the sets of interfaces (110) and $(1\bar{1}0)$, i.e., parallel to $[001]$, that occur in the perovskite blocks occupy positions that are, according to the model, shifted over vectors of the type $\frac{1}{2}[111]_p$ in successive blocks. Since $\frac{1}{2}[111]_p$ is not a superlattice vector the projected traces of

the island interfaces, related by $\frac{1}{2}[111]_p$, do not coincide in HREM images. If the foil thickness is such that several perovskite blocks overlap along $[001]$, complicated high-resolution line patterns may occur. Assuming that successive perovskite blocks are fragmented in the same way they still are related by a pure translation and hence the geometry of the diffraction pattern (i.e., the spot positions) will not be influenced by such shifts. Of course the intensities of the spots will depend on the succession of $\frac{1}{2}[111]_p$ -type shifts between successive blocks. The interface fragmentation in the perovskite blocks can thus most readily be studied on the basis of the $[001]_p$ zone diffraction patterns, possibly assisted by HREM images of very thin samples in which excessive overlap is avoided.

We have seen above that in a number of cases the $[010]_p$ zone image provides an indication as to the perovskite block stacking along $[001]_p$. For instance, in Fig. 10b the projected stacking of the 7-layered lamellae is revealed by the periodic variation of the dot brightness along the layer planes. It suggests a “zig-zag” stacking of the blocks.

Figure 14, made along $[001]_p$, provides a simple example of the complications that can arise depending on the foil thickness; it is obtained from a thin part of a sample, the square island structure being weakly marked by dark lines resulting from a locally wider spacing of somewhat less bright dot rows parallel to the interfaces. The dark lines are clearly double, most probably as a consequence of the relative shifts of successive perovskite blocks. Figure 13b is the image of a similar island structure obtained from a somewhat thicker foil. The interface images are now prom-

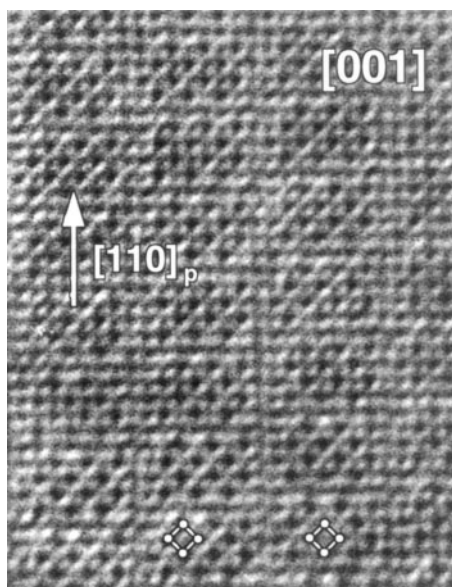


FIG. 25. HRTEM image of a very thin foil in which the atom columns appear as dark dots. At a critical thickness of the wedge-shaped foil dots of two different “darknesses” mark the two different heavy atom columns. Note the spatial phase relationship between the dot patterns in adjacent 5×8 islands.

inently marked by double lines of brighter dots, while the interior of the islands is imaged by somewhat diffuse dots. Such images also suggest that the atomic columns adjacent to the interfaces have a composition different from those in the interior, providing a mode of accommodating deviations from the simple compositions corresponding to the ideal layered structures.

The $[001]$ image of Fig. 25 is obtained from a particularly thin part of the foil. The atomic columns are now imaged as dark dots. Bismuth- and barium-containing columns are imaged as dots of a slightly different “darkness.” In such thin foil the geometry at the interfaces should not be perturbed by overlap. Moreover the darkness is then directly related to the column compositions, i.e., to the column potential. From the location of the darkest dots (which are the minority) it becomes clear that the structures in adjacent 5×8 rectangular islands are out of phase, being related by projected displacements of the type $\frac{1}{2}[110]_p$. Along the interface rows of less dark dots are nearest neighbors; the majority of dots in the unit mesh are of this type. Taking into account that the sample is bismuth rich it seems plausible to conclude that the interfacial regions must be enriched in bismuth.

6.4. Relation between Island Structure and Composition

The idealized geometrical model of Fig. 20 is not adequate in this simple form since it does not give rise to satellites sequences through the origin along $[110]_p$ and $[1\bar{1}0]_p$, whereas such satellite sequences are observed as in Fig. 6. This can be understood as follows: the interfaces can be described as conservative with a displacement vector $\mathbf{R} = \frac{1}{2}[111]$ parallel to the interface, i.e., perpendicular to \mathbf{q} . Such interfaces do not introduce a superperiod in the set of lattice planes with diffraction vectors parallel to \mathbf{q} . However the interfaces are not ideal for several reasons. From the HREM images we concluded that the local interplanar spacing of planes parallel to the interface is about 5% larger than that of the corresponding planes within the islands. Moreover the island formation is apparently composition driven. It is likely that the interfacial region is enriched in the atomic species, which is in excess compared to the composition of the layered structure. It is reasonable to assume that adjacent to the interfaces some of the Ba sites are occupied by Bi, the lone-pair electrons of Bi^{3+} contributing to the local expansion. Also the layer of oxygen along the interface presumably contributes to the local expansion and certainly contributes to the interface image.

6.5. Computer Simulations

In order to support the proposed structure models computer-simulated diffraction patterns and high-resolution images were obtained for various levels of the structures.

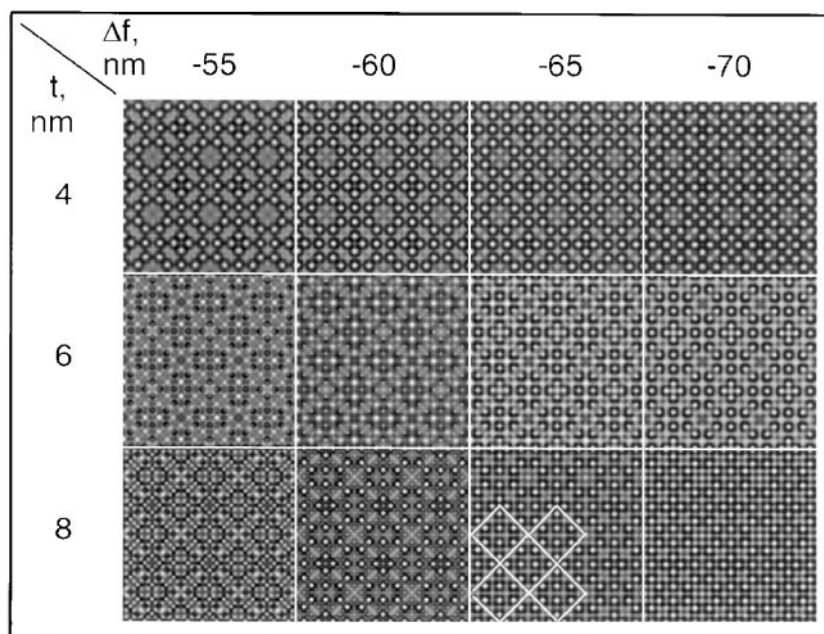


FIG. 26. Matrix of [001] simulated images of a 4×4 island fragmented perovskite lamella (t —thickness; f —defocus) according to the model represented in Fig. 25. The Ba ions in columns adjacent to the interfaces are in part replaced by Bi ions; the interplanar spacing across the interface is assumed to be about 5% larger than within islands. Best fit with the experimental image is obtained for $t = 8$ nm and $f = -65$ nm.

The [010] zone diffraction pattern produced by the basic structure of the 7-layered compound of which a model is represented in Fig. 3 was computed. A comparison of the simulated pattern with the experimental pattern of Fig. 4a, ignoring the weak spots due to the island fragmentation, confirmed that the structure proposed for the idealized 7-layered compound is reasonable. Similar results were obtained for the diffraction patterns of the 5- and 9-layered ideal unfragmented compounds.

The computed [001] zone patterns were the same for all idealized compounds; only spots with $h + k = \text{even}$ are present if the foil contains an integer number of unit cells, confirming the body-centered lattice of the idealized R-P-like structure.

The assumption that under the appropriate conditions two kinds of heavy atom columns can be imaged as dots of different brightnesses in [001] images is crucial for the reasoning used in proposing a model of the island structure. This assumption was found to be justified by simulating the [001] diffraction pattern and the image of the idealized structure of Fig. 20. If the foil thickness is not an integer number of unit cells (e.g., $t = 4.6$ nm) the [001] diffraction pattern contains weak spots with $h + k = \text{odd}$. The corresponding computed image then exhibits bright dots of two slightly different brightnesses for two ranges of defocus values and thickness; best fit is obtained for $\Delta f = -65$ nm, $t = 8$ nm (Fig. 26).

It thus seems justified to deduce the projected unit cells of the superstructures from the repetition periods of the bright-

ness variation of the bright and dark dot pattern; this determines the island size and shape. Also the position relationship between the structures in adjacent islands was deduced on this basis; it leads in the [001] projection to $\mathbf{R}_1 = \frac{1}{2} [110]$ and $\mathbf{R}_2 = \frac{1}{2} [1\bar{1}0]$.

Superstructures in perovskite layers due to coupled tilting of identical undeformed octahedra inevitably produce period doubling but do not lead to fourfold periods along two mutually perpendicular [110] directions. It is thus unlikely that octahedral tilting is solely responsible for the superstructure formation. Models that give rise to diffraction patterns and images with the correct geometry were as a consequence based on combined composition and displacement modulation of an interface fragmented island structure. In particular it is assumed that the heavy atom columns adjacent to the island boundaries are slightly displaced away from the boundaries, increasing the local interplanar distance by about 5%, as suggested by direct spacing measurements on HREM images. Moreover in order to allow for deviations from the ideal heavy ion contents it is assumed that in these columns bismuth atoms substitute for a fraction of 25% of the barium atoms with conservation of the overall fourfold rotation symmetry.

7. DISCUSSION

Two types of models for the unfragmented structures are compatible with the geometry of the ED pattern and with the geometrical features of the HREM images, in particular

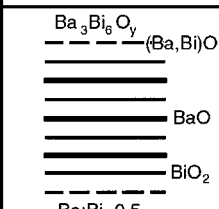
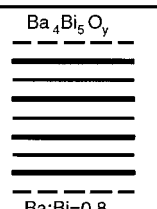
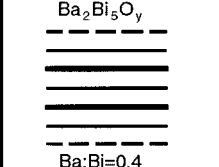
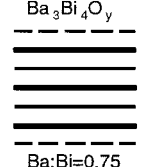
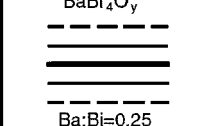
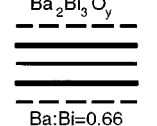
	(a) R-P-like Ba/Bi=n/(n+3)	(b) Alternative Ba/Bi=n/(n+1)
9-layer	$Ba_3Bi_6O_y$ (Ba,Bi)O  BaO BiO ₂ Ba:Bi=0.5	$Ba_4Bi_5O_y$  Ba:Bi=0.8
7-layer	$Ba_2Bi_5O_y$  Ba:Bi=0.4	$Ba_3Bi_4O_y$  Ba:Bi=0.75
5-layer	$BaBi_4O_y$  Ba:Bi=0.25	$Ba_2Bi_3O_y$  Ba:Bi=0.66

FIG. 27. Schematical representation of two possible models for the 5, 7 and 9 layer compounds: (a) the classical Ruddlesden–Popper model; (b) alternative variant of the Ruddlesden–Popper model.

with the configuration of dots in the intermediate lamella. In these models the intermediate lamellae are assumed to be either: (i) a rocksalt-type layer Bi_2O_2 leading to a R–P-like phase (16) or (ii) a calcium fluoride type of layer Bi_2O_4 , leading to an Aurivillius type of structure.

A comparison of simulated images of these models along the $[010]$ and $[110]$ zone axes, with the corresponding experimental HREM images, makes it possible to restrict the possible models to the two variants of type (i) schematically shown in Fig. 27. In both of them sodium chloride-type lamellae are assumed to be present, but they differ by the number of Bi-containing layers. In the R–P-like model (Fig. 27a), this lamella is formed by a cluster of four Bi-containing layers: $\cdots -BiO_2-(Ba,Bi)O-(Ba,Bi)O-BiO_2-\cdots$, in which the BiO_2 layers can alternatively be considered as the limiting layers of the adjacent perovskite blocks.

In the second alternative model the intermediate lamella contains only two Bi-containing layers: $\cdots BaO-BiO-BiO-BaO-\cdots$. The BaO layers are now the limiting layers of the perovskite blocks (Fig. 27b).

The theoretical composition of these idealized layer structures (ignoring island fragmentation and isomorphous substitution) containing n Ba layers is $Ba_nBi_{n+1}O_y$ for the model of Fig. 27b and $Ba_nBi_{n+3}O_y$ for the model of Fig. 27a.

For the interpretation of the experimental HREM images we made the following reasonable assumptions, which are supported by image simulation.

(i) Only heavy atom-containing columns are imaged as dots (i.e., pure oxygen columns do not produce dots);

(ii) Whenever the dot brightness is different for two sublattices of columns, the minority type of dots represents predominantly Ba-containing columns since all compounds contain an excess of Bi over Ba;

(iii) In a restricted area columns having the same composition are imaged as dots of the same brightness.

Under imaging conditions where Bi- and Ba-containing columns are imaged as dots of different brightnesses, this feature should make it possible to distinguish the two models. Unfortunately this simple feature is perturbed by isomorphous substitution of Ba by Bi, making the assignment of columns to a given cation somewhat ambiguous. Moreover, the composition of atom columns parallel to the $[001]$ zone are affected by the $\frac{1}{2}$ $[111]$ displacement between successive perovskite blocks, interchanging at each intermediate lamella the Bi- and Ba-containing columns, leading in projection to equalizing the column compositions, in sufficiently thick foils.

Notwithstanding these restrictions, in thin foils (i.e., containing only a small number of perovskite blocks), subtle differences in brightness in the $[001]$ zone can be observed between the two sublattices of columns parallel to $[001]$. Hence it is possible to deduce the relative shift of the perovskite structure across the interface between two islands. A number of observations is compatible with the assumption that the layered structure consist of unfragmented lamellas since the corresponding ED patterns do not exhibit evidence for a superlattice within the (001) layers. Such cases will now be discussed.

The $[010]_p$ image of the 7-layer compound (Fig. 10b), with an experimentally determined cation ratio Ba:Bi = 0.6–0.65 shows two prominent lines of extra bright dots. Since these brightest dots are the minority species, they most probably represent Ba columns. As such this is not consistent with the 7-layer model of Fig. 3, which would have a local composition $Ba_3Bi_4O_y$, i.e., Ba:Bi = 0.75, and which would require three lines of Ba columns. In order to become consistent as far as composition is concerned one must assume that 1 in 15 Ba sites is occupied by Bi since then $(15 - 1)/(20 + 1) = 2/3$. As to the geometry the observation would be consistent with the R–P-like model of Fig. 27a. However, the ideal composition of Ba:Bi = 0.4 does not agree with the experimental one of 0.6–0.65 unless it is now assumed that isomorphous substitution of 4 in 25 Bi atoms by Ba should occur.

Consistent characteristics, chemically as well as geometrically, are realized in the $[010]$ images of the 9-layer structure such as that Fig. 10c. The minority columns (which should contain Ba) form the sublattice of brightest dots. The observed geometrical features agree well with the alternative model of Fig. 27b. Also the theoretical cation ratio 0.8 fits well with the experimental one of 0.8–0.85. In this particular case model II seems to fit better than model I. Similar conclusions apply to the image

of Fig. 11, even though the contrast is inverted as compared to that in Fig. 10c.

The 5-layer structure produces [010] images such as that in Fig. 10a, which exhibits two lines of extra bright dots in the configuration schematically represented in the model of Fig. 27b, suggesting that the structure of model II predominates. The periodic variation of the dot brightness along the less bright dot lines suggests that the lamellae are island fragmented. The theoretical composition is Ba:Bi = 0.66 to be compared with the experimental one of 0.48–0.52. The two data can be reconciled if it is assumed that 1 in 6 Ba ions is replaced by Bi, making Ba:Bi = 0.5.

The “ideal” island fragmentation is caused by intersecting sets of “conservative” interfaces which do not change the cation occupation of the [001] columns. However the dot pattern in transverse images of sufficient specimens such as Fig. 13b shows that the columns adjacent to the island boundaries often produce dots brighter than those in the columns in the interior of the islands, suggesting that they have a different composition. Small compositional changes from the ideal compositions of the perovskite lamellas can therefore be accommodated along such interfaces; in particular along the intersection lines of the two sets of interfaces atom columns with a singular composition occur. In particular the local oxygen nonstoichiometry can be accommodated in this way.

To the best of our knowledge, the described island fragmented structures constitute a new structure type, in particular illustrating the extraordinary flexibility of perovskite structure to accommodate a wide range of compositions by varying several parameters: number of layers in the perovskite block, nature of the limiting layers of the perovskite blocks, island size and geometry, and presumably vacancies in the island boundaries and finally substitution of Ba by Bi.

8. CONCLUSIONS

The compounds of the type $Ba_nBi_mO_y$, with $m > n$ studied in this paper exhibit a variety of composition-dependent often “local” superstructures that are derivatives of the perovskite basic structure. For well-defined cation ratios with $m = n + 1$ ($n = 2, 3, 4$) it is suggested that the corresponding structures are related to the tetragonal Ruddlesden–Popper phases, i.e., consist of layer-like perovskite blocks joined together by means of (Ba,Bi)O bilayers in a sodium chloride-like configuration. In the structures of compounds with compositions that presumably differ from these simple ones the (001) layer-like perovskite blocks are moreover fragmented in square (4×4 or 5×5) and rectangular islands, e.g., 4×5 , limited by (110) planes, creating a second level of superstructures accommodating these deviations from simple compositions. Excess bismuth seems to substitute for barium in those [001] columns that are adjacent to island boundaries. Along the island boundaries expansion of the interplanar distances is found.

Driving forces for the various ordering patterns may also in part be due to the presence of Bi^{5+} and Bi^{3+} in various proportions in the different compounds. It is moreover difficult to exclude that the oxygen content, in particular the presence of oxygen vacancies, may be in part responsible for the second level of superstructures.

It is realized that the described structures do not always seem to fit the chemical compositions. This is largely due to the fact that ED and especially HREM images tend to determine essentially local structures, whereas the chemical compositions refer to averages over much larger volumes.

We do not claim to have determined unambiguously the complex structures of these compounds, our objective being merely to sketch a building principle that may be useful for further detailed structure determination using complementary, more quantitative approaches, such as X-rays or neutron diffraction.

ACKNOWLEDGMENTS

This work has been performed within the framework of IUAP 4/10. Authors are grateful to N. R. Khasanova and A. M. Abakumov for the helpful discussion.

REFERENCES

1. L. F. Mattheis, E. M. Gyorgy, and D. W. Johnson, *Phys. Rev. B* **37**, 3745 (1988).
2. A. W. Sleight, J. L. Gillson, and P. E. Bierstedt, *Solid State Commun.* **17**, 27 (1975).
3. D. E. Cox and A. W. Sleight, *Acta Crystallogr. Sect. B* **35**, 1 (1979).
4. Pei Shiyong, J. D. Jorgensen, B. Dabrowski, D. G. Hinks, D. R. Richards, A. W. Mitchell, J. M. Newsam, S. K. Sirha, D. Vaknin, A. F. Jawbson, *Phys. Rev. B* **41**, 4126 (1990).
5. D. E. Cox and A. W. Sleight, *Solid State Commun.* **19**, 969 (1976).
6. M. Licheron, F. Gervais, J. Coutures *et al.*, *Solid State Commun.* **75**, 759 (1990).
7. M. Itoh, T. Sawada, R. Liang *et al.*, *Solid State Ionics.* **49**, 57 (1991).
8. K. P. Reis, A. J. Jacobson, and J. M. Nicol, *J. Solid State Chem.* **107**, 428 (1993).
9. L. A. Klinkova, V. I. Nikolaichik, N. V. Barkovskii *et al.*, *Russ. J. Inorg. Chem.* **42**, 1550 (1997).
10. L. A. Klinkova, V. I. Nikolaichik, N. V. Barkovskii *et al.*, *Russ. J. Inorg. Chem.* **44**, 1974 (1999).
11. L. A. Klinkova, V. I. Nikolaichik, L. V. Zorina *et al.*, *Russ. J. Inorg. Chem.* **41**, 709 (1996).
12. F. Abbattista, M. Hervieu, M. Vallino *et al.*, *J. Solid State Chem.* **104**, 338 (1993).
13. C. Michel, D. Pelloquin, M. Hervieu *et al.*, *J. Solid State Chem.* **109**, 122 (1994).
14. S. Esmailzadeh, P. Berastegui, J. Grins *et al.*, *J. Solid State Chem.* **152**, 435 (2000).
15. B. Aurivillius, *Ark. Kemi.* **2**, 519 (1950).
16. S. N. Ruddlesden and P. Popper, *Acta Crystallogr.* **10**, 538 (1957); *ibid.* **11**, 54 (1958).
17. S. Amelinckx and D. Van Dyck, in “Electron Diffraction Techniques” (J. M. Cowley, Ed.), Vol. 2, p. 309, Oxford Univ. Press, New York, 1993.
18. R. Gevers in “Diffraction and Imaging Techniques in Material Science,” (S. Amelinckx, R. Gevers, J. Van Linduyt, Eds.), Vol. 1, p. 9. North Holland Publ. Co, Amsterdam/New York/Oxford.